Synthesis and characterization of P(VDF-TrFE)/Cobalt ferrite composite films

BY

ISRAR AHMED

DEPARTMENT OF PHYSICS

QUAID-I-AZAM UNIVERSITY

ISLAMABAD, PAKISTAN

2023

In the Name of Allah, the Entirely Merciful, the Especially Merciful

Al-Fatihah [1: 1], Nobel Quran

This work is submitted as a dissertation

in partial fulfillment of the requirement for the degree of

MASTER OF PHILOSOPHY

IN

PHYSICS

To The

Department of Physics

Quaid-i-Azam University

Islamabad, Pakistan

2023

CERTIFICATE

This is to certify that the experimental work in this dissertation has been carried out by ***Mr. Israr Ahmed*** under my supervision in the Superconductivity and Magnetism Lab, Department of Physics, Quaid-i-Azam University, Islamabad, Pakistan.

Supervisor:

Dr. Ghulam Hassnain Jaffari
Associate Professor
Department of Physics
Quaid-i-Azam University
Islamabad, Pakistan.

Submitted Through:

Prof. Dr. Kashif Sabeeh
Chairman
Department of Physics
Quaid-i-AzamUniversity
Islamabad, Pakistan.

DEDICATION

To
My Late
Father,
&
My Beloved
Mother

ACKNOWLEDGEMENT

*First and foremost, I would like to praise and thankful to **Allah the Almighty**, the **Most Gracious** and the **Most Beneficent** for his countless blessings and guidance during my whole life. May **Allah's** blessing be upon to His final **Prophet Hazrat Muhammad (Peace Be Upon Him)**, his family, and his companions.*

*Then, I would like to express my sincere gratitude to my supervisor **Dr. Ghulam Hassnain Jaffari** for the guidance, motivation, endless patience, and his immense support during my **M. Phil** study and research. I am grateful for the fruitful discussions that we had. He has given me all the freedom to pursue my research, while ensuring that I stay on course and do not deviate from the core of my research. Without his valuable guidance, this thesis would not have been possible, and I shall eternally be grateful to him for his assistance.*

*I am extremely thankful to my lab seniors **Dr. Fiza Mumtaz** and **Dr. Layiq Zia,** for their guidance and moral support. I deeply appreciate the help and time they have given; their guidance was advantageous throughout my research work. None of the work presented in this thesis would have been possible without the generous support of all my friends, family, and colleagues. I would also like to express my sincere gratitude to my lab fellows specially **Muhammad Shahid Iqbal Khan, Hafsa Shawana & Sumbal Amin,** who always helped in my practical work**.** My appreciation also goes to my colleagues **Musfira Aqeel, Eisha-tur-Razia, Aqsa Idrees, Muhammad Salman, & Farwa Saleem** for all the help, friendly and working environment during my research work.*

*I would like to pay heartfelt thanks to my late father. My words can't explain my heart feelings for my late father who always prioritize my higher education. But Alas! This time my father is not with me, but I hope so that he is seeing me from the heaven. **(May ALLAH grant him highest place in Jannah)**. Also, I would like to thanks' my beloved mother whose prayers always give me potential and energy, whenever I was fed up with the hardships of life.*

I would also like to thank my dearest family. Thank you to my niece "Anaya Masood", mother, brothers, and sister. Thank you for enduring difficulties of long

distances throughout my M.Phil and providing me with unwavering support. My achievements are your achievements, and they could not be possible without all your sacrifices and support throughout the years. I strive to make you all proud.

Izrar Ahmed

ABSTRACT

In this work, PVDF-TrFE/$CoFe_2O_4$ nanocomposite free standing films are prepared, and their multiferroic properties are studied. These properties include structural, optical, magnetic, and ferroelectric properties. $CoFe_2O_4$ nanoparticles synthesized by the cost-effective sol gel method. Free standing PVDF-TrFE/$CoFe_2O_4$ nanocomposite films with varying $CoFe_2O_4$ content have been prepared using solvent casting (or drying casting method). Structural analysis of all prepared films is done by PANalytical X-Ray Diffractometer. Effect of adding cobalt ferrite (CFO) nanoparticles in PVDF-TrFE matrix is delicately observed and analyzed in detail. The crystallinity of the films is affected by the incorporation of cobalt ferrite nanoparticles into Poly Vinylidene trifluoride P(VDF-TrFE). Ferroelectric response at room temperature is studied by measuring polarization versus electric field loops at low frequency 10 Hz and high frequency 400 Hz. Some PVDF-TrFE films exhibited saturated ferroelectric hysteresis loops, which show that the addition of TrFE monomers induced a high content β-phase. For low CFO concentration, good ferroelectric response has been achieved. While for higher concentrations, non-saturated ferroelectric hysteresis loops are observed in PVDF-TrFE/CFO films, which confirm lossy capacitive behavior. The effect of $CoFe_2O_4$ nanoparticles on the polarization has also been analyzed in detail. An increase in saturation polarization is observed with the addition of $CoFe_2O_4$ nanoparticles, attributed to the interfacial effects and interactions between nanoparticles. Fourier transform infrared spectroscopy reveals presence of the beta-phase in all composite films. Reflectance is measured against energy reveals presence of d-d transition associated with the CFO particles. Temperature dependent magnetic response is also observed which show ferromagnetic behavior. Both temperature dependent magnetization and hysteresis behavior have been presented. Data has been analyzed on the bases of Bloch's law.

Table of Contents

List of figures:

List of Tables:

1 Chapter 01 Introduction and Background

1.1 History of polymers:

The word "polymer" was put forward by the Swedish chemist "J. J. Berzelius". He said that Benzene (C_6H_6) is the polymer of Ethyne (C_2H_2) [1, 2]. Natural polymers have been used for many decades. It was felt around the globe that polymer materials were colloids. "Staudinger" in 1920s introduce the concept of polymer [2]. He observed and then described by saying that "lots of small molecules that were interacting strongly with each other". He was first that said that "a polymer is made up of very large molecules, called macromolecules". Atoms of the molecules were held together by covalent bonds. A new field called polymer science deals with natural and synthetic fibers, plastics, rubbers, coatings, adhesives etc. Polymers have even more uses than you could visualize. They are used in solar cells, food and medicine packaging, drug delivery, adhesives, textile, auto parts and toys [3].

1.2 Dielectrics:

Dielectric is extract from the prefix "dia", means "through" or "across"; thus, the dielectric is defined as a material that allow the passage of the electric field or electric flux, but not particles (i-e., electrons) [3]. A "dielectric" material store energy when external electric field is applied. Polarization can be produced when electric field is enforced in dielectric material. Due to applied electric field, charges slightly supersede from their equilibrium position, resulting in dielectric polarization. Positive charges move along the direction of applied field while negative charges move opposite to applied field. Dielectrics can be classified as polar dielectric (e.g., water molecule) and nonpolar dielectric (e.g., carbon dioxide) [4]. Due to applied electric field charge separated in parallel plate capacitor as shown in Figure 1.1.

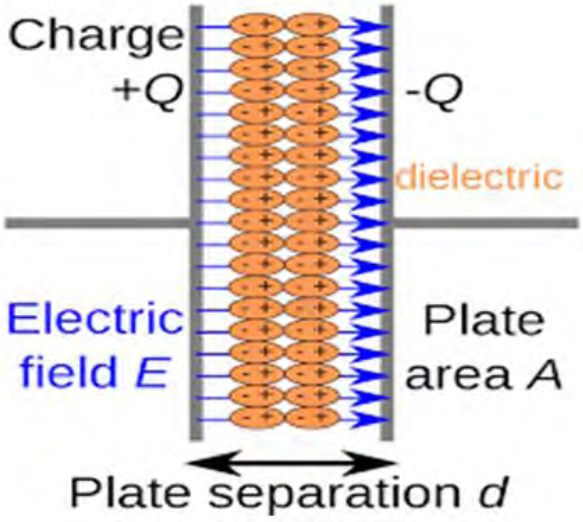

Figure 1.1: Separation of charges due to applied electric field in a parallel-plate capacitor [5].

Dielectric constant ε comprises of a real part ε' representing the storage of electrical energy, and an imaginary part ε", describe the loss or energy absorbed. The loss factor includes the effects of both dielectric loss and conductivity. Permittivity describes the interaction of a material with an electric field "E" and is a complex quantity [6].

$$\varepsilon = \varepsilon' - i\varepsilon" \qquad (1.1)$$

1.3 Polarization:

When a capacitor is exposed to an external electric field, the dielectric material becomes polarized. Anions in the material align themselves towards positive electrode, and the cations shift towards negative electrode. Overall polarization of a dielectric material appear from the sources of charge displacement: ionic displacement, space charge displacement, electronic displacement, the orientation of permanent dipoles and hopping [7].

1.4 Mechanisms of polarization:

Following are some of the mechanisms of polarization that occur in dielectrics.

1.4.1 Ionic polarization:

When any dielectric material is placed in applied electric field, polarization occurs due to the movement of cations and anions, is called ionic polarization. Ionic polarization

is produced only in ionic substances. When an electric field is enforced to ionic materials, cations and anions separate from each other, which results in the net dipole moment. The equation which described the mechanism of ionic polarization given below [8].

$$p_{av} = \alpha_i E_{loc} \qquad (1.2)$$

where "p_{av}" is average dipole moment, "α_i" is ionic polarizability, "E_{loc}" is the localized electric field. Figure 1.2 shows that when the electric field is zero polarization is zero but when the electric field in applied in leftist direction ions distorted in the direction of enforced field and due to this polarization is not equal to zero.

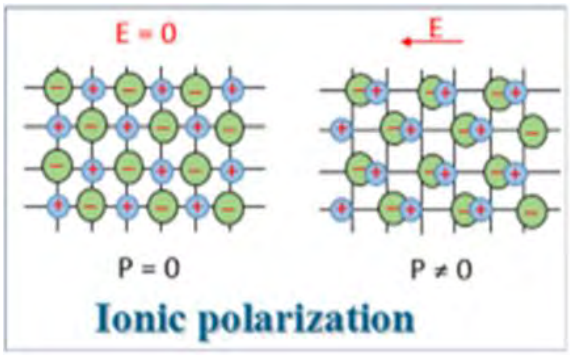

Figure 1.2: Schematic illustrations of ionic polarization [9].

1.4.2 Space charge polarization:

Space charge polarization is also entitled as “interfacial polarization”. When the low-frequency electric field is applied, charges move through a certain distance within the material. When these moving charges are impeded, space charge polarization arises due to metal or dielectric interface collection of charges. Due to the cumulation of charge at the interface, field distortion occurs, which increases the capacitance of a material, i-e; there is an increase in the dielectric constant. This kind of polarization arises in materials exhibiting high conductivity, i-e., materials with high concentrations of mobile charges (free electrons or ions). Phenomenon of space charge polarization is presented in Figure 1.3.

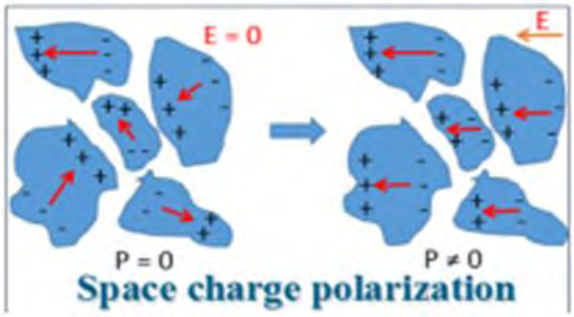

Figure 1.3: Simplified illustrations of space charge polarization [9].

1.4.3 Electronic polarization:

Electronic polarization occurs within the dielectric material when there is a slight shift in the positive and negative charge in the opposite direction due to electric field application. Polarization can be measured by electric dipole moment, which can be calculated by multiplying the distance between distorted charges with the magnitude of one of the charges. Phenomenon of electronic polarization is shown in Figure 1.4. If "p_{av}" is the average dipole moments and "E_{loc}" is a local field at which atoms or molecules are polarized, then average dipole moments proportional to a local domain and given by as [10];

$$p_{av} = 4\pi\varepsilon_0 r^3 E_{loc} \qquad (1.3)$$

Where "r" is the distance between two charges.

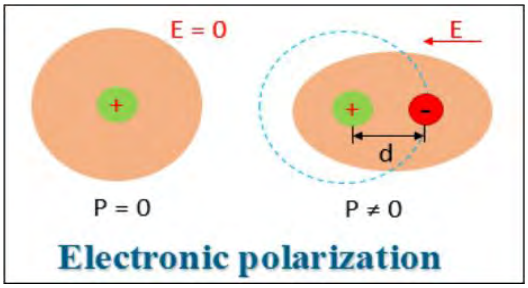

Figure 1.4: Schematic illustrations of electronic polarization [9].

1.4.4 Orientational polarization:

It occurs only to polar dielectric materials. In the absence of electric field, electric dipoles are oriented randomly such that their net effect becomes zero due to which polarization is zero. These dipoles try to rotate and orient in the direction of applied electric field as shown in below Figure 1.5. This is known as orientational polarization.

The average dipole moment, in this case, is temperature dependent, and an electric field can be obtained using Boltzmann's statistics.

$$P_{av} = \frac{P^2}{3k_B T} \qquad (1.4)$$

where "P" is the dipole moment of one molecule, "E" is electric field, and "k_B" is Boltzmann constant [11].

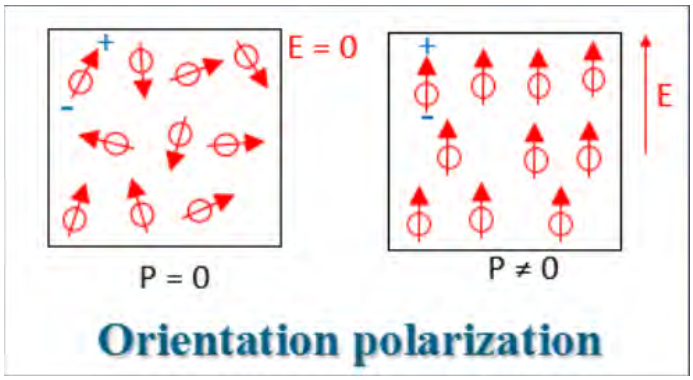

Figure 1.5: Orientational polarization mechanism in dielectric materials [9].

1.4.5 Hopping polarization:

In dielectric materials, the localize charges i-e holes and electrons can jump from one site to another for a short interval of time. When these localized charges are trapped in this site for longer, hopping polarization occurs. Phenomenon of hopping polarization is shown in Figure 1.6 in which a charge hops from one place to another place.

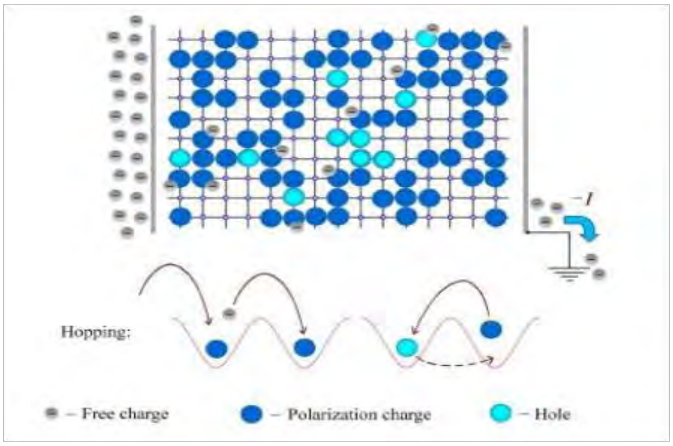

Figure 1.6: Schematic illustrations showing hopping polarization.

Deformed polarization is also known as resonance process as it imply vibrating modes and this phenomenon appeared as a peak in the dielectric constant and frequency

curve. While the orientational, hopping, and space charge polarization take longer over a wide range compared to electronic and orientational polarization (>10^{-5} sec). These polarization phenomena are also termed relaxation processes, which involve dielectric relaxation. Relaxation occurs when we apply an electric field; the electric dipoles orient in some specific orientation, but when we reverse the direction of applied field, the dipoles don't have sufficient time to orient themselves along the direction of field. So, the time these dipoles take to reorient themselves along the direction of field applied is known as relaxation time. Occurrence of different polarization mechanisms as a function of time with electric field as a step function is shown in Figure 1.7.

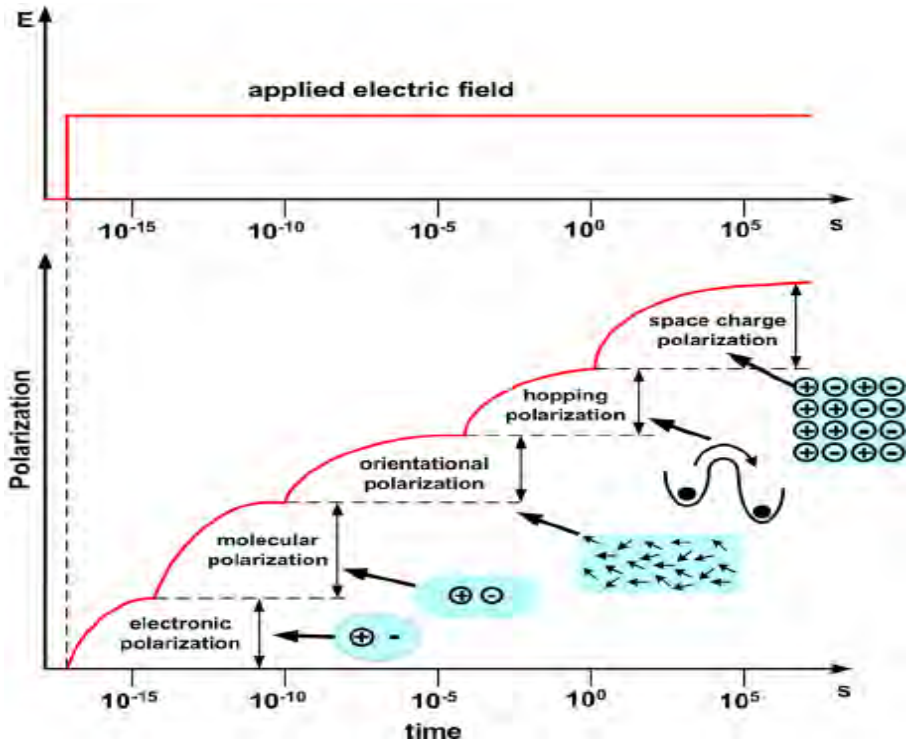

Figure 1.7: Response of a generic material to polarization with respect to time and electric field as a step function [12].

1.5 Effect of different parameters on dielectric constant:

The dielectric constant varies in the dielectric materials with the variation of temperature, structure, and applied frequency. These parameters are explained below:

1.5.1 Effect of temperature:

The dielectric constant strongly varies with the increase or decrease of temperature, causing discontinuities in the dielectric constant. Those materials which have permanent

dipoles have a significant effect on temperature and on their dielectric constant. When we give enough thermal energy to permanent dipoles, dipoles start the migration, moving in a random direction concerning the field. Subsequently, the dielectric constant decreases. In multiferroic materials, steady dielectric declines with the increase in temperature because of inverse relation between them. This occurs at Curie temperature because at this temperature, a phase transition occurs, i-e., the materials go from ferroelectric phase to para-electric phase [13].

1.5.2 Effect of structure:

Like temperature, the dielectric constant also depends upon the form of material. Polar materials with permanent dipoles have a higher dielectric constant than nonpolar materials. When different mechanisms of polarization act simultaneously, there will be a large resultant dielectric constant. In polymers, when the chains are mobile, there will be low crystallinity; as a result, steady dielectric increases [14].

1.5.3 Effec of the electric field:

When the dielectric material is exposed to electric field, four phenomena can occur conduction, polarization, breakdown, and dissipation. Normally a dielectric material is an insulator, but there are certain charges inside the dielectric material, and due to this, the material possesses leakage current. If the material has a stable surface with area A, thickness d, then the conductivity of a material is [15]:

$$\sigma_{dC} = \frac{Id}{vA} \tag{1.5}$$

Good insulating dielectric conductivity could be as small as 10^{-18} S/m [16].

In capacitors, when the A.C electric field is applied, two types of current flow through the material: the polarization current, and the conduction current. Polarization current flows through capacitive saving energy, while the conduction current produces resistance dissipation energy. If the surface of electric material is "S" and the thickness is "d", then polarization current and conduction current is:

$$I_P = i\omega\varepsilon_0\varepsilon_r' SE_0 e^{i\omega t} \tag{1.6}$$

$$I_c = \omega\varepsilon_0\varepsilon_r'' SE_0 e^{i\omega t} \tag{1.7}$$

1.5.4 Effect of frequency:

When an electric field is applied to dielectric material, dipoles starts to orient themselves in the direction of applied field. At low frequency range, dipoles easily align in order of applied field, and the dielectric constant increases. At high frequency, the molecules cannot line up in the order of applied field, because they don't follow the field change. Due to this phenomenon, the dielectric constant decreases. Variation in dielectric parameters i.e., dielectric constant and dielectric loss as a function of frequencies is shown in below Figure 1.8.

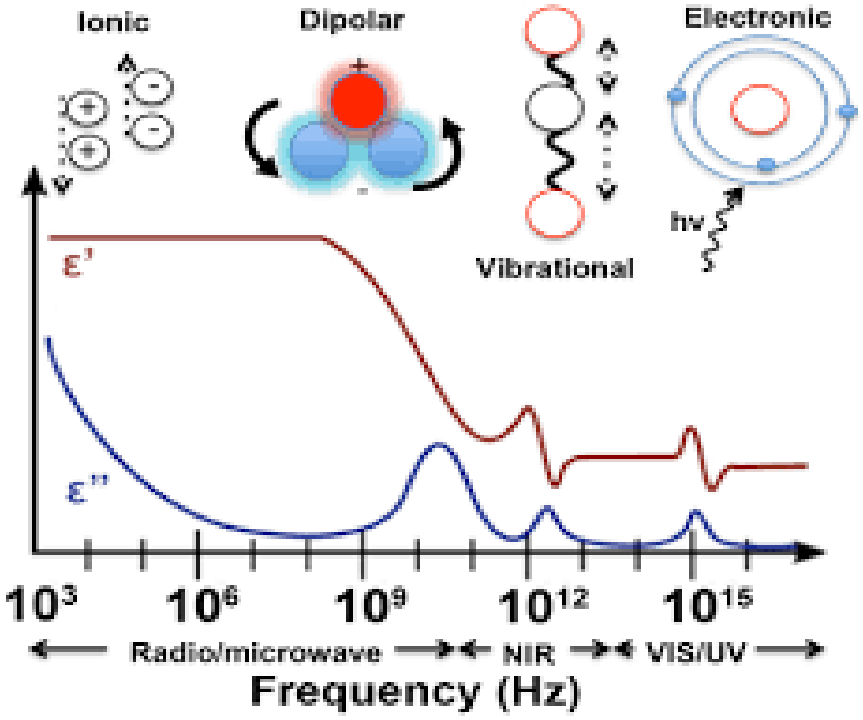

Figure 1.8: Dependency of (1) Relative dielectric constant on the frequency of an alternating electric field (2) Relative loss factor on the frequency of an alternating electric field. Contributions of electronic, dipolar, ionic and vibrational in the total polarization are determined [17].

1.6 Ferrites:

Ferrites are composed of oxides of magnetic materials in which ferric ions are the main component. Word ferrite comes about from Latin word "Ferrum," that is used for "iron" [18]. Ferrites are ceramic materials with black or dark grey color, brittle and hard in nature.

1.7 Spinal Ferrites:

The chemical formula of spinel ferrite is AB_2O_4, where A can be any divalent metal ion. Spinel ferrites possess a cubic closed packed structure where oxides ions are packed in a face-centered cubic [FCC] arrangement. Crystal structure of spinel ferrites contains two positions, namely tetrahedral [A] and octahedral [B] [19]. Due to the variation in the placement of cations and anions at both locations, spinel ferrites have numerous engrossing properties. Metal ions are tetrahedrally coordinated with oxygen at 8 [A] sites, while oxygen ions are octahedrally coordinated at 16 [B] sites. Fundamentally the localization of two sites depends on the occupying lattice and the ion size [20].

1.8 Ferrimagnetic ordering in spinal ferrite:

Magnetically, spinel ferrites show ferrimagnetic ordering. At both "A" and "B" sites, magnetic moments of cations are oriented alongside with each other. The arrangement between the "A" and "B" sites, is antiparallel, as there are double as many "B" sites as "A" sites, so net moment of spins gives us ferrimagnetic ordering in the crystal. Inverse spinel structure is shown in Figure 1.9.

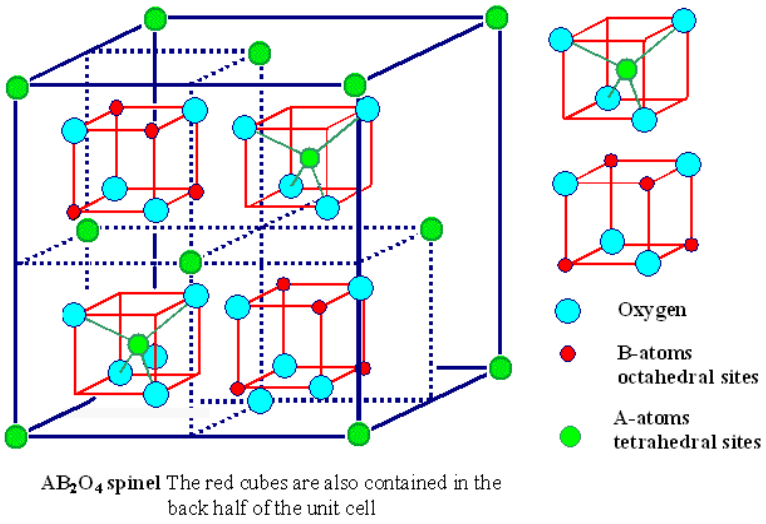

Figure 1.9: AB_2O_4 Inverse Spinel structure [21].

1.9 Types of spinel ferrites:

Following are some types of spinel ferrite based on crystal structure and magnetic properties.

1.10 According to crystal structure:

Spinel ferrites consist of following two types on the base of crystal structure:

1.10.1 Normal spinel ferrites:

In normal spinel ferrite structure, [8] tetrahedral lattice sites are populated by metal di-valent ions, while sixteen octahedral lattice sites are populated by tri-valent iron ions. These spinels have chemical formula $(M^{2+})^{A}[Fe_2^{3+}]^{B}O_4^{2-}$, where "Fe" is the tri-valent ion and "M" is the di-valent ion. Examples of normal spinel ferrite is $MgAl_2O_4$ and $FeCr_2O_4$ [22]. Normal spinel structure of AB_2O_4 is shown in Figure 1.10.

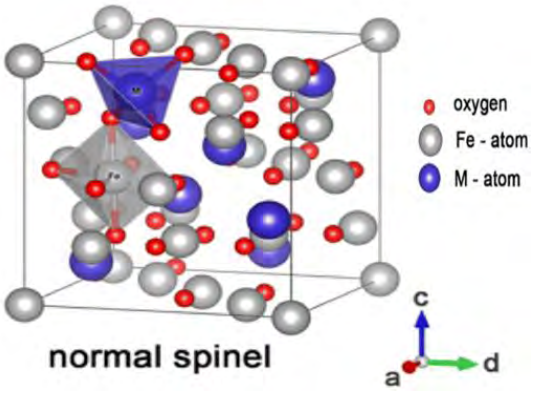

Figure 1.10: Crystallographic structure of AB_2O_4 normal spinel structure [23].

1.10.2 Inverse spinal ferrites:

In inverse spinel ferrite, all the metal cations occupied the [A] sites while half of the iron cations occupied tetrahedral [B] lattice sites, while the other half occupied the octahedral lattice sites [24]. Structure of inverse spinel of AB_2O_4 is shown in Figure 1.11.

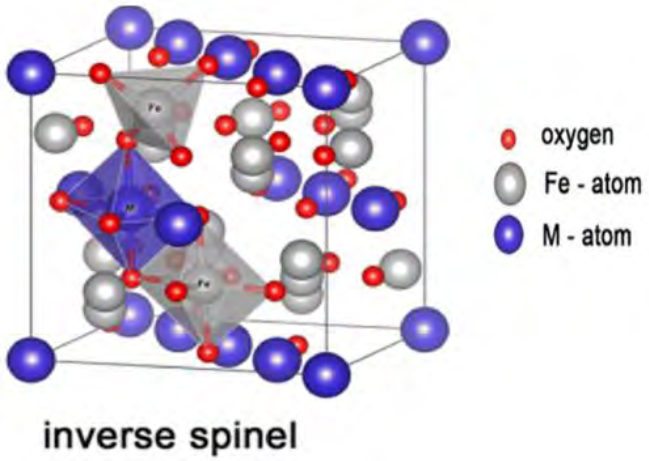

Figure 1.11: Crystallographic structure of AB_2O_4 inverse spinel structure [23].

Table 1.1: Occupancy of sites in Inverse and Normal Spinels [22].

Site	Similar Interstices (per unit cell)	Number Occupied (per unit cell)	Cation arrangement (Inverse Spinel)	Cation arrangement (Normal Spinel)
Octahedral (B)	32	16	8 Fe^{3+} 8M^{2+}	16 Fe^{3+}
Tetrahedral (A)	64	8	8 Fe^{3+}	8 M^{2+}

1.11 According to magnetic properties:

Ferrites, one that has a low coercivity of magnetization, and hard ferrites, one that has a high coercivity of magnetization.

1.11.1 Soft ferrites:

Ferrimagnetic materials that don't retain magnetism after being magnetized are called soft ferrites. The hysteresis loop of soft ferrites is narrow and small with fewer energy losses as shown in Figure 1.12, while the magnetization curve has a steep rise in magnetization [25]. These ferrites can be produced by soothing, cooling, and heating, which can be easily magnetize and demagnetize. Soft ferrites are ceramic nonconductor or insulator with different crystal structures have high susceptibility and permeability value. Soft ferrites are used in telephone signal transmitters, electromagnets, cores of transformers, computer data storage, receivers etc.

1.11.2 Hard ferrites:

When the ferrimagnetic materials become magnetized, they retain their magnetism called as hard ferrites. These materials are also called permanent magnetic materials with gradually rising magnetization curves, large energy losses during magnetization and large hysteresis loop [26]. These ferrites can be fabricated by sudden cooling and heating, which can't be easily magnetized or demagnetized. These ferrites have high coercivity and retentivity, low susceptibility and permeability, high saturation flux density and high eddy

current losses. Therefore, hard ferrites are used in loudspeakers, DC and permanent magnets etc., [27]. Hysteresis loop of hard ferrites are shown in Figure 1.12.

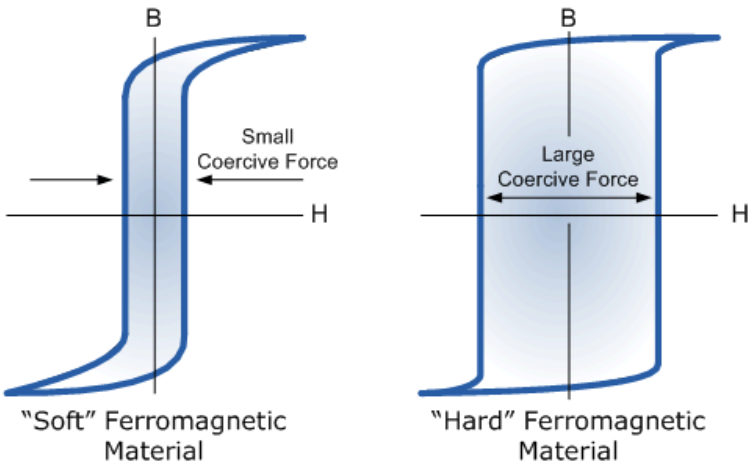

Figure 1.12: Hysteresis curve for hard ferrites (right) and soft ferrites (left) [28].

1.12 Ferroelectricity:

Certain materials have spontaneous polarization property that can be reversed back by applying the external field [29]. Ferroelectric materials are crystals in which structural units are electric dipoles. This means that the center of the positive and negative charge is slightly displaced or separated in each unit cell. Each dipole moment of the unit cell is oriented with its neighboring unit cell in the lack of an external electric field. Several types of domains in unit cell are randomly oriented; therefore, net dipole moment will vanish. When external field is enforced, randomly oriented domains starts to align themselves along applied field. Below a certain temperature ferroelectricity arises known as Curie temperature T_c. Above Curie temperature, ferroelectric material becomes para electric because heat agitates the dipoles so that the forces that align the dipoles vanish [30]. Due to applied electric field polarization changes direction as shown in Figure 1.13.

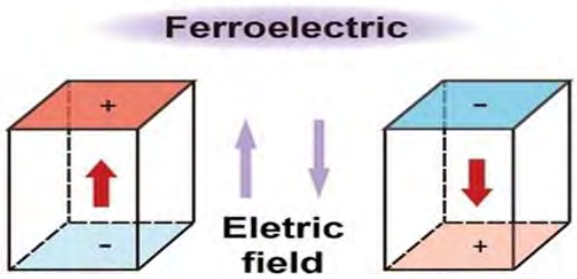

Figure 1.13: Inversion of polarization by applied electric field [31].

1.12.1 Ferroelectric Phase Transition:

Ferroelectric materials are polar and exhibit spontaneous polarization below a critical temperature T_c. When temperature exceeds the critical temperature T_c the material transforms from ferroelectric to para electric and becomes nonpolar. Due to this spontaneous polarization, crystal structure changes, known as a ferroelectric phase transition [32]. Above T_c material loses all its ferroelectric characteristics. When phase transition occurs, new properties arise in the material. Phase transition can be happened due to the change in pressure, temperature, and other thermodynamic variables.

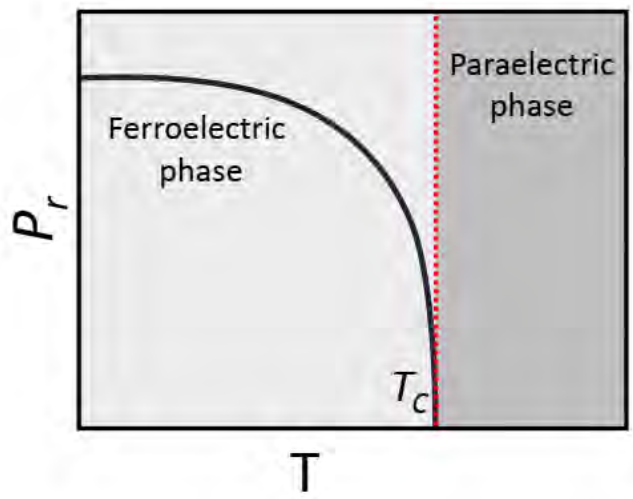

Figure 1.14: Variation of P_r as a function of temperature in ferroelectric materials [33].

Ferroelectric crystal shows spontaneous electric polarization at certain temperature range called Curie temperature. Ferroelectric materials shows high dielectric constant near Curie temperature [34]. At T_c dielectric constant increases rapidly and reaches a high peak value. This steady dielectric increase at Curie temperature is called anomalous behavior. By Curie Weiss relation:

$$\varepsilon(T > Tc) = \frac{C}{T - Tc} \qquad (1.8)$$

where "T" is temperature measured in Kelvin, "C" the material specific Curie constant.

Figure 1.15 shows the phase diagram of PVDF-TrFE. Ferroelectric phase ordering is achieved when T_c is below T_m. There is no change in the crystallite size when the melting temperature, T_m, remains the same. When annealing is performed at a temperature above

T_m both paraelectric and ferroelectric phases are modified. This phenomenon is shown by the appearance of one paraelectric and one ferroelectric phases in below Figure 1.15.

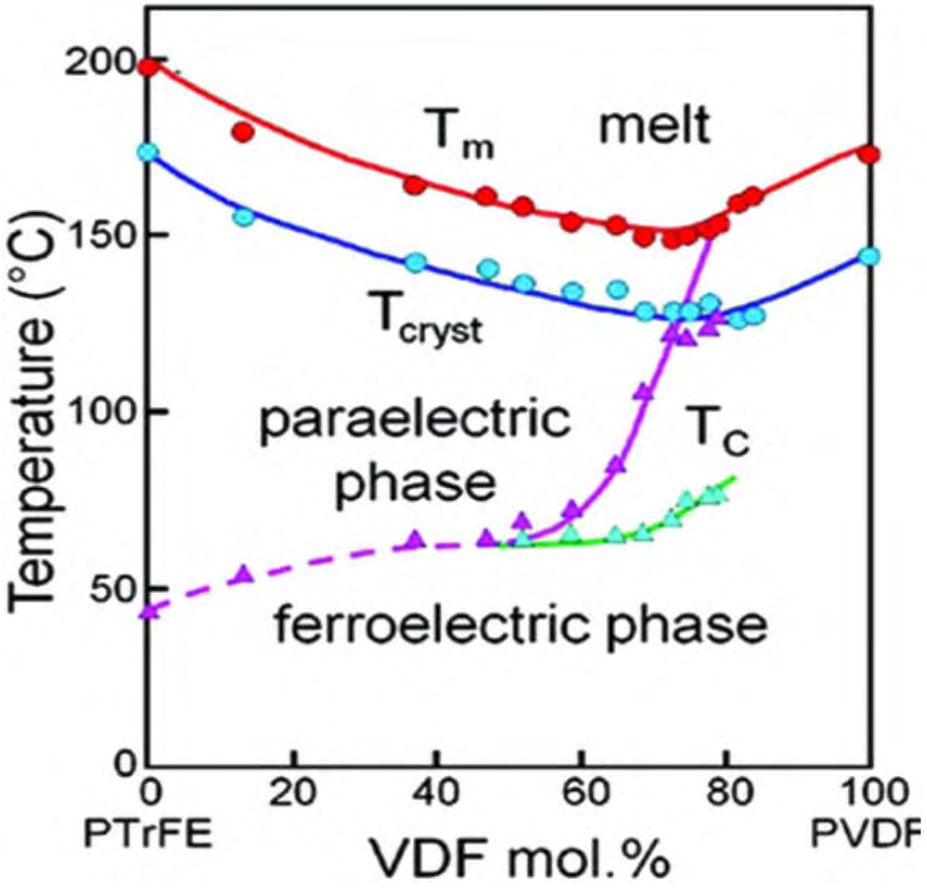

Figure 1.15: Phase diagram of traditional P(VDF-TrFE) [35].

1.12.2 Ferroelectric Hysteresis Loop:

Just like ferromagnetic materials, ferroelectric materials exhibit a hysteresis loop. We know that ferroelectrics are the class of materials that retain their polarization even after the eviction of an electric field [36]. Figure 1.16 shows that increase in electric field results increase in polarization means the electric domains were randomly oriented before applying electric field. But when the strength of field is high, these electric domains start to orient along the direction of field. A stage comes when further increase in the electric field does not affect electric environment because all the electric domains are aligned, and all the backgrounds are saturated.

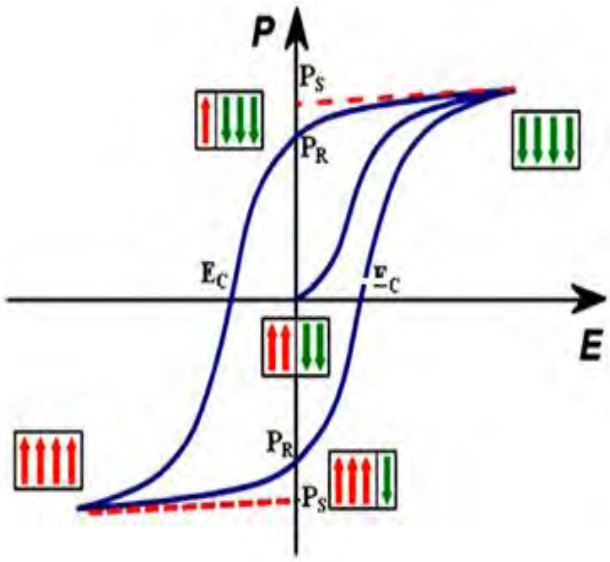

Figure 1.16: Hysteresis (P-E) curve in ferroelectric materials [37].

1.13 Poly (vinylidene-triflouroethylene)/P(VDF-TrFE):

P(VDF-TrFE) is semi-crystalline copolymer which is obtained with the combination of vinylidene fluoride VDF ($CH_2.CF_2$) and tri-fluoroethylene TrFE (CHF-CF_2). Molecular structure of P(VDF-TrFE) is shown in Figure 1.17. It's Curie temperature (T_c) is lower than it's melting temperature (T_m), which varies from 55-128 °C, depends on the amount of TrFE [38]. Copolymers have various chemical ingredients with vinylidene fluoride (VDF) contents ranging from 50-80 mol% at room temperature. Ferroelectric property in copolymers occurs due to the crystalline ß-phase in which all polymer chains are in Trans (TTTT) conformation while all fluorine atoms are unilateral in the chain [39].

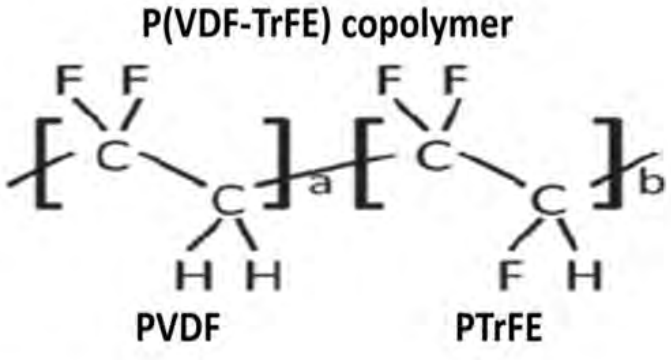

Figure 1.17: Molecular structure of P(VDF-TrFE) [37].

Suppose the molar content of trifluoro ethylene TrFE is less than 20%. In that case, it attracts absorption because they materialize or crystallize directly into ferroelectric ß-phase, and exhibit ferroelectric or paraelectric phase below the melting point [40]. P(VDF-TrFE) oligomer molecular model is shown in Figure 1.18(a) while electron clouds are schematically shown in Figure 1.18 (b).

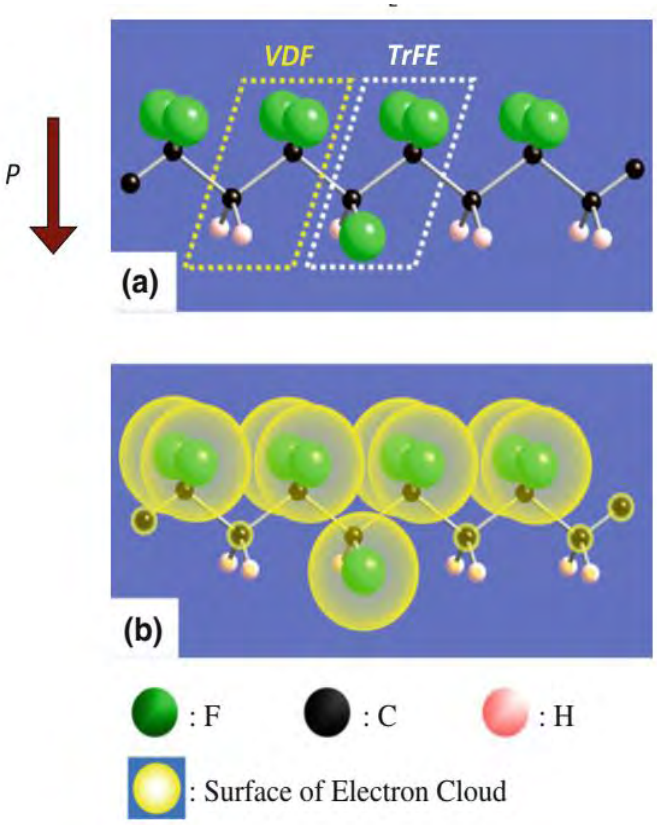

Figure 1.18: The molecular model of a P (VDF-TrFE) oligomer [41].

1.14 Phases in P(VDF-TrFE):

Based on the crystallization, copolymer shows the following three phases.

1.14.1 Alpha Phase:

The alpha phase is the nonpolar phase (trans-gauche conformation, TGTGTG). Lattice parameters of α-phase are a = 4.96 Å, b= 9.64 Å, and c = 4.62 Å [42]. The crystallization from the melt normally brings about to the nonpolar α-phase. The α-phase of PVDF can be remold into the γ-phase through thermal treatment and into the δ-phase through poling under high electric field [43]. In this phase, molecular chains are aligned antiparallel to each other as shown in Figure 1.19, which are nonpolar. In this phase, every

second molecular chain is rotated at an angle of 180°. α-Phase exhibits a monoclinic structure due to its symmetry, even though all the angles in its unit cell are 90°. Alpha conformation is thermodynamically unstable, making the transition from beta to alpha difficult.

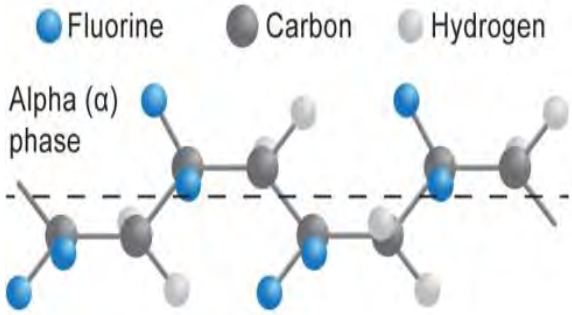

Figure 1.19: Chemical structure of alpha phase conformation.

1.14.2 Beta Phase:

The beta phase is the polar phase that exhibits a high dielectric constant of all polymer phases. β-phase have lattice parameters, a=8.58Å, b=4.91Å, and c=2.56 Å [44]. β-phase exhibits orthorhombic structure. Due to trans-planar zig-zag (TTTT) conformation, β-phase has largest spontaneous polarization [45]. β-phase displays the best ferroelectric, piezoelectric and ferroelectric properties. β-phase PVDF can be made by stretching the α-phase PVDF or poling α and γ PVDF under even higher value of electric field. β-phase is thermodynamically stable that's why it can be easily achieved in P(VDF-TrFE). Chemical structure of β-phase conformation is show in below Figure 1.20.

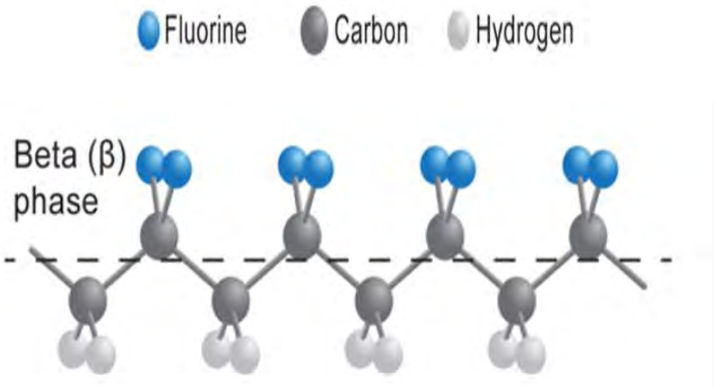

Figure 1.20: Chemical structure of beta phase conformation.

1.14.3 Gamma Phase:

γ-phase is third crystalline phase in PVDF with (TTTG-TTTG′) conformation. It's lattice parameters are a = 4.97 Å, b = 9.66 Å, and c = 9.18 Å [46]. γ-phase PVDF can be acquired from high-temperature crystallization. It's structure is orthorhombic which is similar to the β-phase crystal [47]**.** γ-phases show a smaller dipole moment than that of β phase.

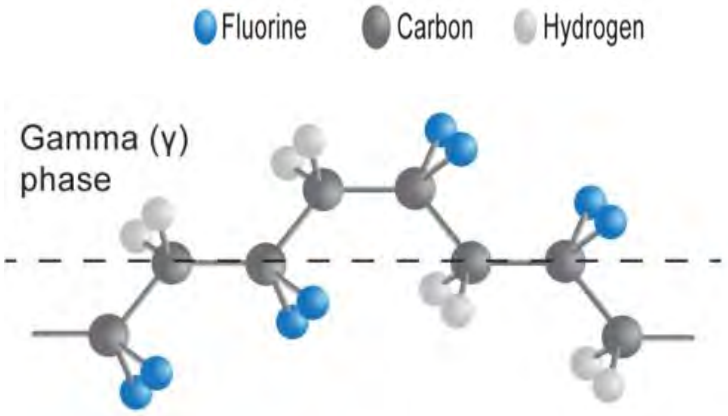

Figure 1.21: Chemical structure of gamma phase conformation.

1.15 Ferroelectricity in P(VDF-TrFE):

In P(VDF-TrFE), ferroelectricity emanated from vinylidene fluoride (VDF). Ferroelectricity can be controlled by the quantity of "TrFE" added to polymer (PVDF). Ferroelectricity can be achieved maximized with the addition of small amount of "TrFE". Because the dipole moment arises from the TrFE monomer.

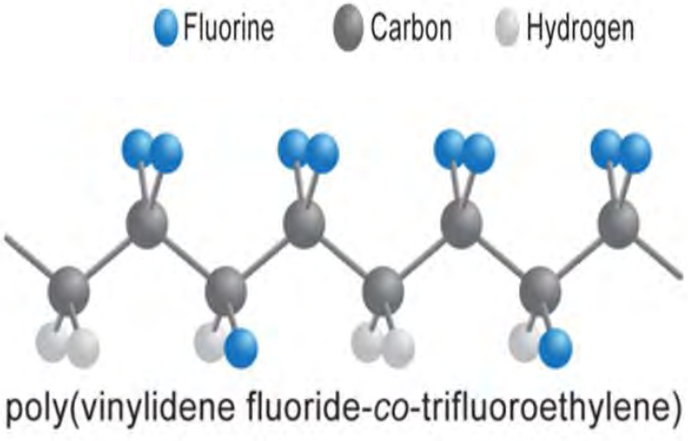

Figure 1.22: Chemical structure of PVDF-TrFE.

1.16 Cobalt Ferrite:

Cobalt ferrite is a ceramic material with chemical formula of $CoFe_2O_4$ ($CoO \cdot Fe_2O_3$). It is considered between the soft and hard magnetic material due to semi-hard nature. CFO belongs to the space group Fd3m, with lattice parameter a=8.38 Å. Cobalt ferrite is a ferrimagnet with a Neel temperature of 800 K. Cobalt ferrite ($CoFe_2O_4$, CFO) is the representative of the spinel ferrite family [48]. Cobalt ferrite (CFO) has great chemical and physical stability, large anisotropy, making it applicable for bio-medical requisitions. Magnetic property arises due to tetrahedral and octahedral sites. The $CoFe_2O_4$ is suitable material in chemo resistive sensor, pathogenic detection, storage, dye degradation and energy harvesting. Besides these features, it has utilizations in MRI, sensors, drug delivery, biotechnology, and tissue repair [49]. $CoFe_2O_4$ inverse spinel structure unit cell and subunits are shown in below Figure 1.23.

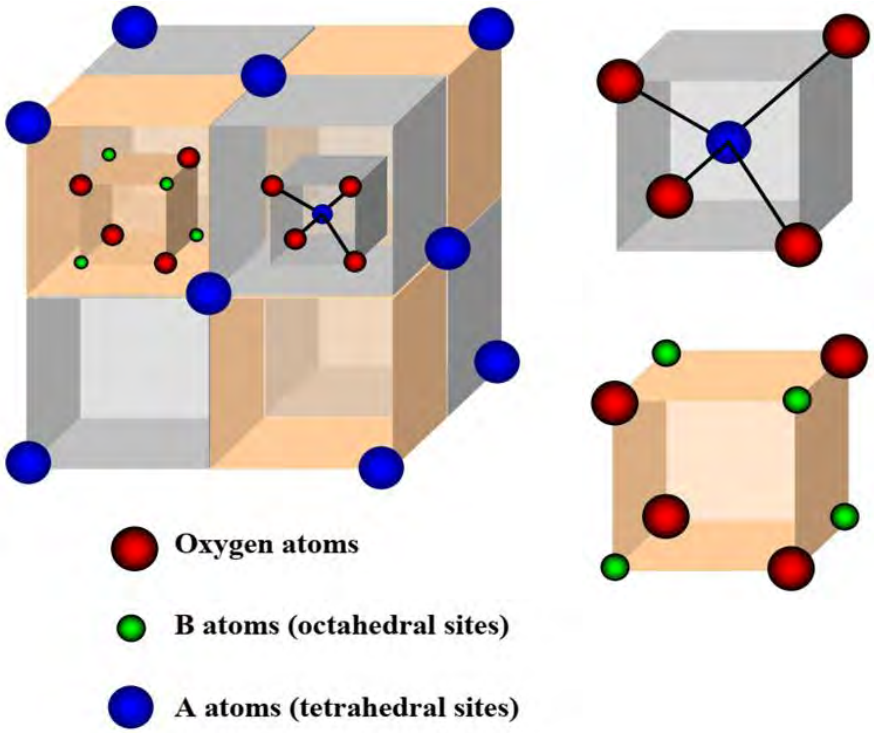

Figure 1.23: Diagrammatic illustration of the unit cell and subunits in $CoFe_2O_4$ [23].

1.16.1 Structure of Cobalt Ferrite:

Cobalt ferrites possess a chemical formula $CoFe_2O_4$ with an inverse spinel structure. It has high degree of magnetic anisotropy and magnetostriction. Its crystal structure can understand its unique electrical and magnetic properties. When Co^{2+} lies on the octahedral

site while Fe^{3+} ions lie on the tetrahedral site, its structure will be inverse spinel. While, normal spinel structure, A^{2+} cations occupy tetrahedral lattice sites, whereas B^{3+} cations occupy the octahedral lattice sites [50]. In spite of that, inverse spinel structure octahedral coordination lattice sites are occupied by half A^{2+} cations, and the B^{3+} cations occupied by the remaining half of the tetrahedral coordination sites [51]. In Figure 1.24 tetrahedral sites are occupied by Fe^{1} cations in orange, while octahedral site is occupied by Fe^{2} ions in gold.

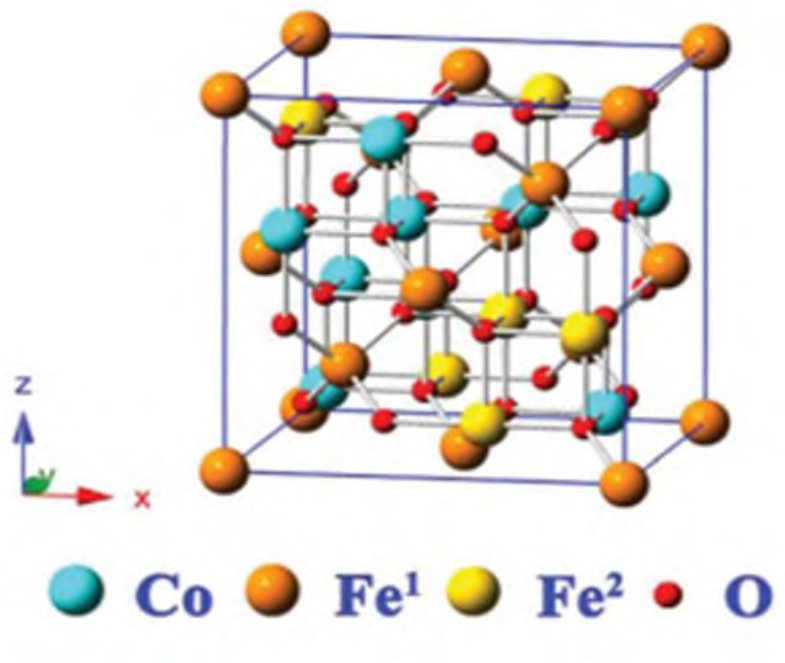

Figure 1.24: Crystal structure of inverse spinel cobalt ferrite. Ball & stick model illustrate Fe^{1} cations at A-sites in orange, Fe^{2} cations at B-sites in gold, Co cations as blue spheres and O anions in red[52].

1.16.2 Magnetization in CFO:

CFO have high degree of magnetic anisotropy and considerable anisotropic magnetostricition ($\lambda 100 = -590\times10^{-6}$ and $\lambda 111 = -120\times10^{-6}$) that's why it is the rarest compound in many spinel ferrites make it appealing magneto strictive candidate in composite multiferroics [53]. In $CoFe_2O_4$ tetrahedral sites contain eight Fe^{3+} ions aligned antiferromagnetically with octahedral sites that has eight Fe^{3+} and Co^{2+} ions per unit cell. CFO is a promising candidate as a spinel phase in self-assembled multiferroics for providing the strong magneto striction to enhance magneto-electric coupling [54].

1.17 Literature review:

Incorporating different nanofillers in the copolymer matrix, results in promising electrical, magnetic, and optical properties [55]. Following are some of the characterization results which are reported in the literature:

The structural characterization of P(VDF-TrFE) and CFO composite films is presented in many research articles. All peaks are identified as P(VDF-TrFE) and cobalt ferrite nanoparticles peaks. A sharp peak around 20° specify the copolymer peak indicating the (110) and (200) atomic planes, whilst all other peaks are ascribed to the cobalt ferrite phase. This reveals that nanoparticles are completely embedded in P(VDF-TrFE) matrix. Nanoparticles are poly-crystalline and have no specific crystal orientation [56].

The XRD pattern of CFO nanoparticles which have reflection in (111), (220), (311), (222), (400), (422), (511), (440), (620), (533) and (622) planes which are well consisted with card (PDF#22-1086) [57]. XRD pattern of P(VDF-TrFE) and CFO composite films with distinct ferrite concentration shows peak at 20.4° coincide with β-phase of copolymer. The intensity of CFO peaks increases with the increase of filler concentration, while the intensity of the copolymer peak decreases significantly [57].

The PE loops of P(VDF-TrFE)/CFO composite films are described in many research articles. The PE loops with varying CFO concentration were computed at room temperature, f=1 Hz and E=30MV/m. The maximal values of polarization P_{max} are 5.6, 11.1, 6.2, and 7.4 mC/m^2 for P(VDF-TrFE), CF 5, CF 10, CF 15 and CF20, samples respectively. Highest value P_{max} reaches in sample CF 10 [58].

P(VDF-TrFE) hyteresis loops loaded with varying concentration of $CoFe_2O_4$ nanoparticles (CFN) showed increase in polarization value. P(VDF-TrFE) film gives maximum polarization (P_{max}) 0.13 μC/cm^{-2}, whilst composite films show polarization P_{max} of 0.3 μC/cm^{-2} for P(VDF-TrFE). Addition of CFO nanoparticles instigate more free charges in polymeric composite films, due to which polarization domain is stabilized [59, 60]. Polarization process enhance the ferroelectric properties of the polymer matrix. Sample with 10% CFN emanate 8% low P_{max} value as compared to the sample containing 5% CFN. Ferrite contents above 8% may diminish dipole chains of the polymer, which leads to the decrease in P_{max} [61].

Magnetic hysteresis loops of composite films are reported in plenty of research articles. Values of M_r, M_s, and H_c are , 20.1, 77.6 emu/g, and 1023 O_e. These values of the CFO nanoparticles are comparable to the value of bulk magnetization 80.9 emu/g [62]. This proves that nanoparticles have good ferromagnetic valuables. Furthermore, M_r values of composite films are 1.4, 2.2, 3.8, and 4.7 emu/g and the M_s values are 3.9, 7.9, 11.5, and 15.2 emu/g, for CF5, CF10, CF15, and CF20 samples. Value of magnetization of composite films enhance with the increase in cobalt ferrite concentration.

FTIR pattern of 0.95P(VDF-TrFE) and 0.05CFO composite thin films shows specific bands of alpha-phase at 766 cm^{-1} and beta-phase at 840 cm^{-1}. Beta-phase fraction is calculated by applying the below relation.

$$F_\beta = \frac{A\beta}{(K\beta/K\alpha)\, A\alpha} + A_\beta \qquad (1.9)$$

where "A_α" and "A_β" shows absorbance at 840 and 766 cm^{-1}, respectively, F_β represents the β-content and "K_α" and "K_β" and are the absorption coefficients at the respective wave number [63]. 53% β-content is calculated in the thin film.

The saturation magnetization of CFO nanoparticles powder sample is above 62 emu/g. When the magnetic nanoparticles dispersed with varying concentration in composites, inside the polymer matrix, values of saturation magnetization of ferrite particles fit well. Measured hysteresis loops shape exhibit that nanoparticles are maximally dispersed inside the polymer matrix [64].

Room temperature magnetic hysteresis loops were measured by "VSM" Lakeshore, Model 7300 series. Applied magnetics field was perpendicular to the surface of composite films. Magnetic hysteresis loops of samples are measured with field of 12 kOe. Maximum magnetization value outreach 52 emu/g which is nearly to cobalt ferrite nanoparticles synthesized by various techniques [65, 66].

The magnetic curves of nanocomposite films and CFO nanoparticles computed at room temperature. The maximum value of magnetization of CFN, obtained by plotting M vs. $1/H^2$ was summed up 47.6 emu/g. Coercivity value was in the range of 3 kOe, compatible with cobalt ferrite. The maximum magnetization was consistent with the addition of cobalt ferrite in the composite, whilst coercivity varies in the range of 3 kOe.

Copolymer loaded with 4, 8, 12% CFN show a saturation magnetization of 12.5, 19.7, 27.4 emu g^{-1}. These values indicate that saturation magnetization correspond with the CFN content [67, 68].

When magnetic field is applied along out of plane or in-plane (perpendicular or parallel) to the surface of cobalt ferrite films, we disclose that strength of magnetic field and temperature have significant effect on magnetization. Values of M_s and M_r are 85.6 and 44 emu/cm^3 obtained when CFO film is annealed at 800°C, i-e., when the temperature rises from 500 °C-800 °C, under a magnetic field of 1.5T. This indicate that maximum crystallization of CFO come up with magnetic property. Enhancement in magnetization is based on the concentration of cobalt ions in spinel lattice [69].

1.18 Motivation:

When at least two ferroic orders (ferroelectric, ferromagnetic or ferroelastic) combines, multiferroic or magnetoelectric materials formed. These materials have applications in fields such as modulation of amplitudes, switching of polarization, waveguides, sensors, and transducers. The main purpose of our present work is to fabricate P(VDF-TrFE)/CFO films with enhanced ferroelectric and magnetic properties. To obtain optimal properties, homogeneous dispersion of CFO nanoparticles in P(VDF-TrFE) matrix with minimum particle agglomeration is very important [70-72].

In recent years, plenty of research has been done to upgrade the dispersion of nanofillers in polymer matrix by using surface functionalization technique [73, 74]. The main challenge is to break the nanoparticles agglomeration and prepare composite film with well dispersed filler while maintaining the properties of composite film. Also, addition of more than a specific amount of filler can disturb the chain alignment and as a result reduce the β-phase content. Therefore, an optimum concentration of filler is also necessary to achieve maximum magnetic and ferroelectric properties.

Poly (vinylidene fluoride/trifluoroethylene) copolymer contain maximum VDF content have been extensively studied for their fascinating ferro-electric properties. Including that piezoelectric and pyroelectric characteristic, PVDF, which is a crucial ingredient for the synthesis of magnetoelectric composites exhibit phase transition (ferroelectric-paraelectric). This transition occur when critical temperature is below the melting temperature. Copolymers exhibit improved ferroelectric properties when PVDF is

crystallized from melt [75, 76]. Among all the phases of PVDF, β-PVDF is most polar and exhibits highest ferroelectricity compared to other phases. But this phase is very difficult to achieve in PVDF homopolymer and has many critical issues. Introduction of TrFE monomers to PVDF, results in direct crystallization to β-phase [77].

Our aim is to prepare homogenous P(VDF-TrFE)/$CoFe_2O_4$ composite films with well dispersed fillers without any surface functionalization and to find an optimum concentration of filler at which maximum dielectric and ferroelectric properties can be achieved. In this work, cost effective solvent casting technique was used, and to ensure the homogeneous dispersion of nanoparticles with minimum agglomeration, stirring time and solution viscosity were optimized.

2 Chapter 02 Experimental Techniques

Different experimental techniques are carried out for the characterization of the prepared samples. Following are some techniques that are explained in this chapter.

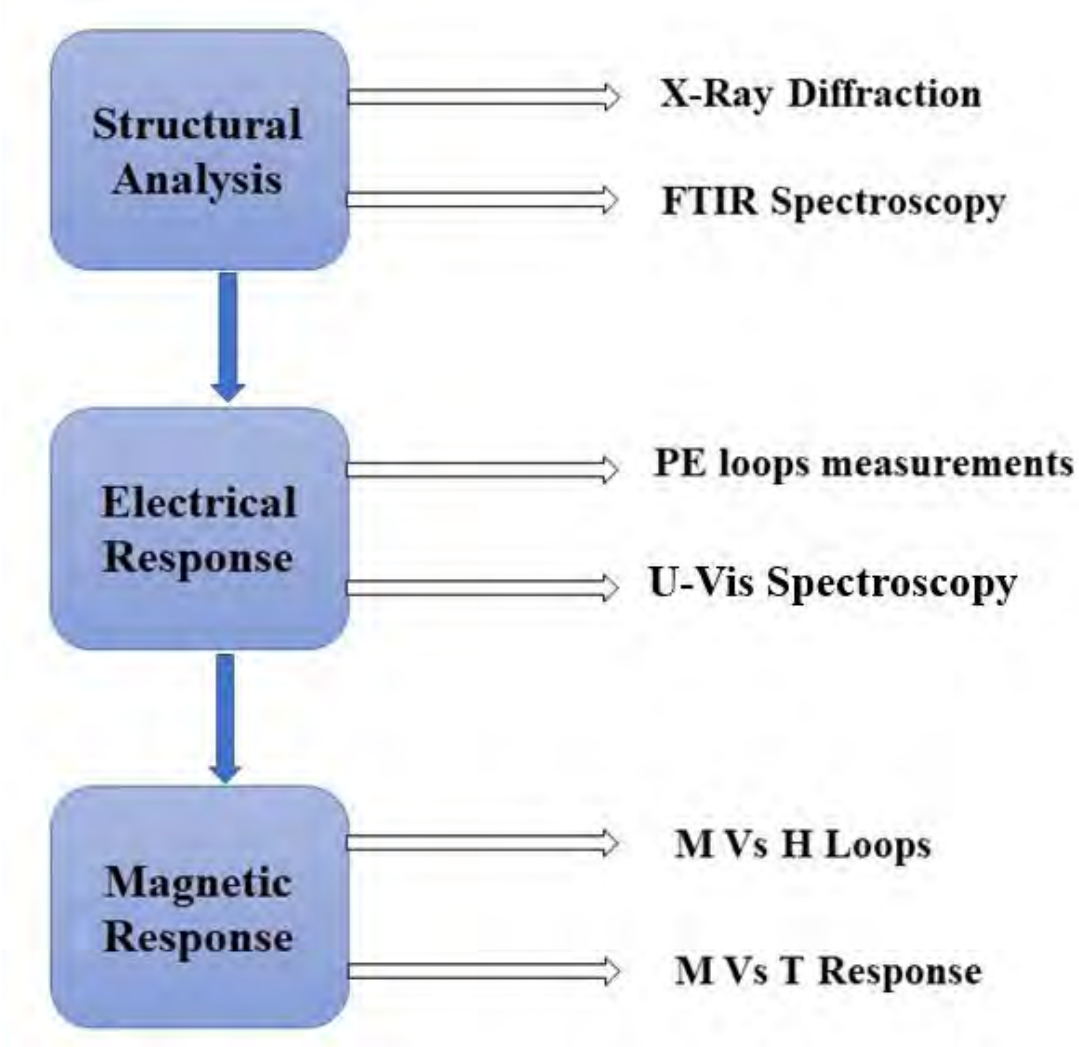

Figure 2.1: Flow chart of the characterization techniques that are taken for my work.

2.1 X-Ray Diffractometer:

X-rays were discovered by the German Physicist "Roentgen" in 1895. To investigate the crystallographic structure of the material, we use the x-ray diffraction technique because the wavelength of x-rays (**λ**) is comparable (1Å) to the interplanar spacing (d). XRD analysis identifies materials based on their phase identification and diffraction

pattern. XRD also yields information on how the actual structure diverge from the absolute one, as a result of defects and internal stresses.

2.1.1 Working Principle of XRD:

We know that a regular array of atoms forms a crystal. When x-rays interact with the atom's electrons, x-rays are scattered by crystal atoms. This anomaly is called elastic scattering, and electron is called a scatterer. A regular group of electrons produces an ultimate collection of spherical waves. These spherical waves go in every direction and interfere constructively and destructively. In some specific rules, they interfere constructively and added while most x-rays interfere destructively and cancel each other. Bragg's law describes this whole phenomenon and is shown in Figure 2.2:

$$2\,d\sin\theta = n\lambda \qquad (2.1)$$

where "θ" is incident angle of x-rays, "d" is interplanar spacing, "λ" is x-rays wavelength and "n" is an integer. Those specific directions in which beams interfere constructively appear as a spot. Consequently, we get a diffraction pattern due to the impinging of electromagnetic waves (x-rays) on a regular array of scatterers.

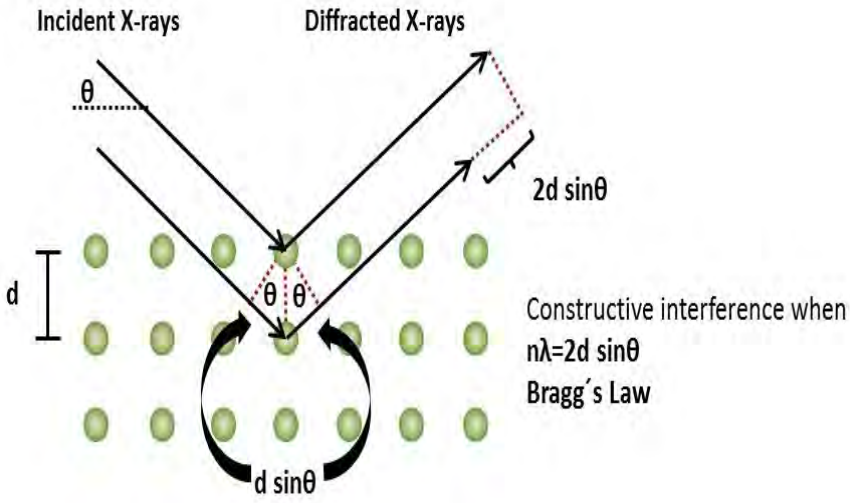

Figure 2.2: Schematic view of Bragg's law Reflection [78].

2.1.2 Structural Analysis:

In our laboratory, all XRD scans were performed using a PANalytical Empyrean System. The main constituents of an X-Ray Diffractometer are an X-Ray tube with Copper (Cu) as an X-Ray source, X-Ray detector, sample holder, and a computer control system.

The characteristic wavelengths of X-Rays from the Cu source are Kβ~1.54187 Å, Kα1~1.540593 Å and Kα2~1.54442 Å. The operating voltage for the PANalytical Empyrean system is 40 kV, and the operating current is 40 mA. The specimen, X-ray source, and counter lie in the same plane. In this work, XRD data is taken within the range of 10^{o}-80^{o}, with step size of 0.02^{o} and stay time of 2 sec. Bragg Brentano geometry is used in the current analysis with fixed divergence slits.

Figure 2.3: Photograph of PANalytical EMPYEREAN XRD in Magnetism lab QAU.

2.2 Polarizations vs. Electric field (P-E) loop measurement:

Polarization is induced when there is alignment of fixed or induced dipole moments along the direction of applied electric field. Studying the phenomenon behind that how atoms or molecules react to an external electric field is polarization. Change in the value of electric polarization with respect to applied electric field is called hysteresis loop.

2.2.1 Sawyer Tower circuit:

Sawyer and Tower, in the 1930s, carried out the first studies on measuring hysteresis loops. P-E hysteresis loops of the ferroelectric material is calculated by using the below ferroelectric tester. Across the ferroelectric specimen electric field is applied, also known as ferroelectric capacitor, determined by the charge on the ferroelectric

specimen by integrating the current across the reference capacitor, which is connected in series with the specimen. Therefore, the charge on the reference capacitor is assumed to be equivalent to the charge on our specimen. The charge on the ferroelectric capacitor, determined by using the relation:

$$Q_0 = V_y C_0 \qquad (2.2)$$

where "V_y" is the voltage across the reference capacitor and "Q_0" number of charges stored on reference capacitor "C_0". The charge stored on each capacitor must be the same. When two capacitors are connected in series; charge on the reference capacitor and ferroelectric specimens are same because the ferroelectric illustration is connected in series with the reference capacitor. Both the voltages are supply into an oscilloscope's X and Y-axes to generate the Polarization vs electric field loop. Diagrammatic demonstration of Sawyer Tower circuit used for ferroelectric hysteresis measurement of film is shown in below Figure 2.4.

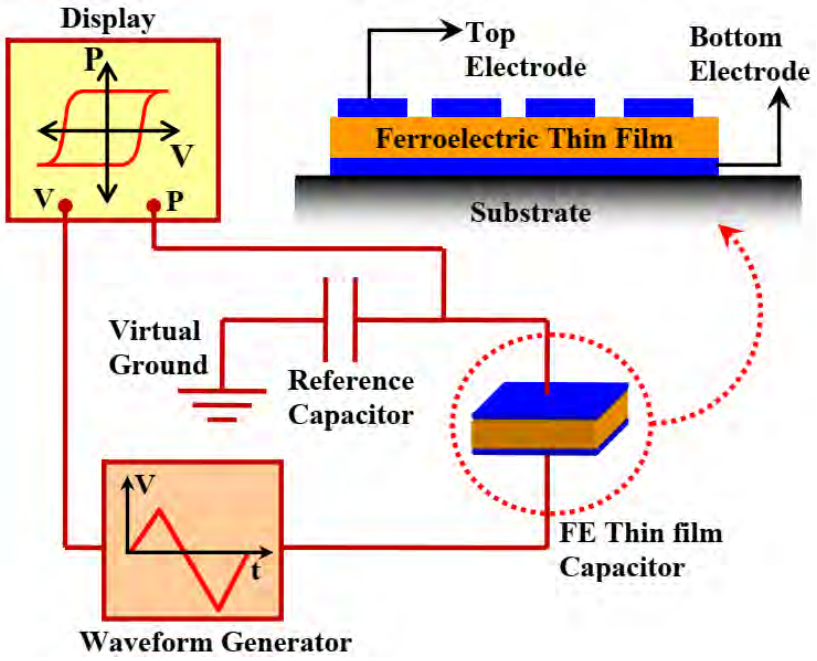

Figure 2.4: Schematic diagram of Sawyer Tower circuit for hysteresis loops measurement of thin films [79].

In this work, P-E loops measurements were performed using PolyK Polarization Loops and Dielectric Breakdown Test System, shown in Figure 2.5.

Figure 2.5: PolyK Polarization loop and Dielectric Breakdown Test System.

2.3 Fourier Transform Infrared Spectroscopy (FTIR):

In FTIR technique, infrared (IR) radiation beam is used to identify functional groups of materials (solid, liquid and gas). Infrared spectroscopy technique compute the incorporation of infrared radiation made by each molecule bond. As a result, this displays a spectrum commonly consigned as transmittance (%) versus wave number (cm^{-1}). To determine the functional group of the molecule, this should be IR active means molecule has some dipole moment. IR radiations interact with the covalent bonds of the materials. As a result, molecule absorbs energy, and the adhesives vibrate in back-and-forth oscillation. Exchange in net dipole moment of the molecule is caused by these oscillations, and the molecule must absorb infrared radiations.

Symmetrical molecules single-atom don't absorb Infrared radiations as the former has no net dipole moment, and the latter have only a single bond. As every bond has some specific vibrational frequency, so a particular infrared radiation frequency will be absorbed.

Figure 2.6: Nicolet 5700 FTIR Spectrometer.

2.3.1 Sample Preparation for FTIR:

Preparation of sample is predominant for Infrared spectra analysis. Infrared radiations are strongly assimilated in glass materials and plastics. The cell or sample holder comprises of ionic substances i-e., potassium bromide (KBr) or sodium chloride (NaCl). Plates of KBr are costly but superior over the NaCl plates as KBr plates take down the infrared spectra from 400-4000 cm^{-1} while the economical NaCl plates take spectra in the range of 650-4000 cm^{-1}. First, we grind the KBr powder with the addition of acetone for about 45min to 60 min. After that, we made two pellets of KBr by giving a pressure of 4 tons through a hydraulic press. Then we place our sample between two pellets and place those pellets in the cell or sample holder. Some carbon dioxide (CO_2) and water (H_2O) present in the aerosphere typically appear in the compound spectrum. So before proceeds to the spectrum of our samples, we first run the background spectrum, which produce complications during elucidation of spectrum. Background spectrum is subtracted from the compound spectrum.

Table 2.1: Numerous functional groups range in wave number (cm^{-1}).

Range (cm^{-1})	Functional Groups
2500–3000	Carboxylic (O-H)
2260–2220	Nitrile (CN)
3010–3100	(=C-H) stretch
1620–1680	(C=C) stretch
1750–1680	Ketone C = O
3500–3500	O = C – N - H stretch
2950–2850	C-H stretch
1740–1690	Aldehyde C = O
3200–3550	O - H stretching

2.3.2 Working Principle of FTIR:

Infrared spectroscopies operate on the principle, that molecules absorb specific frequencies which are quality of their structure. A lionizing black body source emits beam of IR rays. This beam then drifts through an aperture which controls the number of IR rays entering the detector. Then this beam throw into the interferometer where spectral encoding occurs, and the subsequent signal leaves the interferometer. After that beam plunge into compartment of sample, where it is pass on to the sample's surface. Here specific frequencies, distinctive characteristic of the sample, are pass on. Finally, the detector takes down the beam and provoke a signal for final calculation. That signal is digitalized and redirect to the computer where Fourier transformation takes place. Schematic illustration of simple spectrometer layout is shown in Figure 2.7.

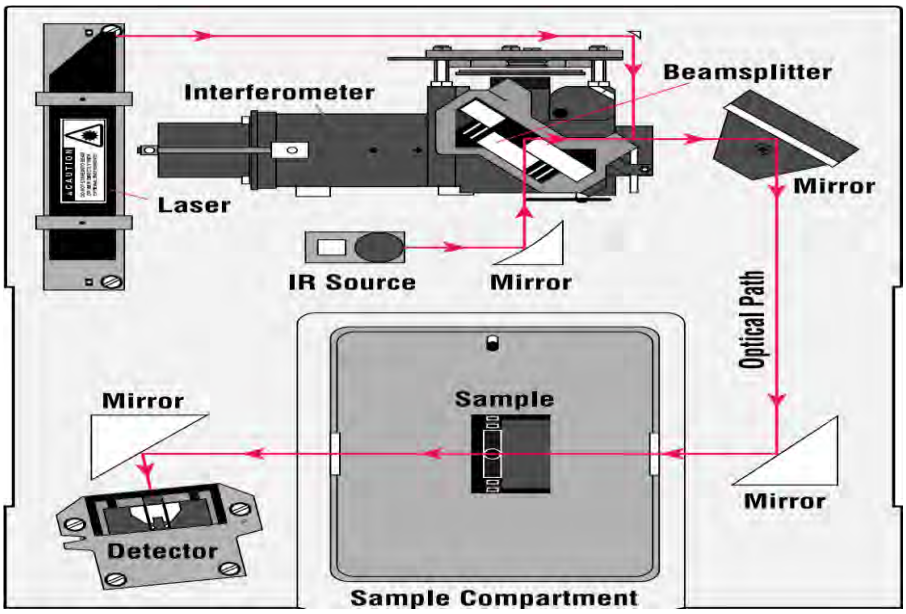

Figure 2.7: Simple spectrometer layout.

2.4 U-Vis Spectrometer:

For the optical measurements of the samples (specially band gap) we use the Lambda 950 spectrometer setup. It is a versatile spectrometer operating in the UV-Visible spectral range. It also operates in the near IR (NIR) region. Lambda 950 is shown in Figure 2.8, and it consists of:

- Double monochromator
- Double beam

- Ratio recording optical system
- Double monochromator
- Ratio recording optical system
- Lamp & detector compartment
- Connector panel

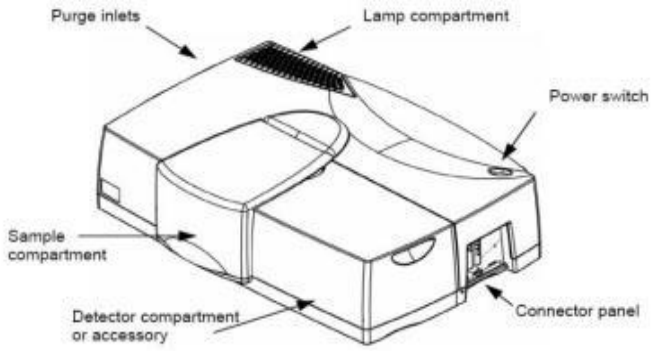

Figure 2.8: Features of Lambda 950 spectrometer.

All optical constituents are coated with silica for permanence. Holographic gratings are handed-down in each monochromator for the ultraviolet and near infrared range. It has double beam and double monochromator for removing the background signal.It utilizes two radiation sources, a halogen lamp (HL) and deuterium lamp (DL) and it cover the operating wavelength range of spectrometer. Photomultiplier tube and PbS act as detectors. Its resolution is up to 0.05 nm and wavelength range is 175-3300nm. All the optical compartments are also sealed which helps to protect them from dust or fumes.

2.5 Vibrating Sample Magnetometer:

Vibrating Sample Magnetometer "VSM" is used to evaluate or quantify the magnetic properties of composites. It is a elementary yet constructive technique for characterizing properties of magnetic materials introduced by "S. Foner" [80]. VSM measures the magnetic properties of materials like, solids, powders, single crystals, liquids, and thin films [81]. Vibrating Sample Magnetometer setup allows to probe experimental technique for estimating properties of magnetic material such as saturation hysteresis, coercivity, and anisotropy.

2.5.1 Working of VSM:

VSM consists of non-magnetic rod connects the sample to the vibrating driving head, which is then positioned in a zone of DC magnetic field produced by an electromagnet as shown

in Figure 2.9. A compatible magnetic field induce a magnetic dipole moment in the sample. The sample is vibrated sinusoidally by the vibrator, which is parallel to applied DC magnetic field. The sample is set down in the middle of the detection coils, which are made up of two counter-round pick up coils. The received signals are directly related to the amplitude of the sinusoidal motion, frequency, magnetic moment of the vibrating sample and geometrical factor such as surface area of detecting coils and their distance from sample [82].

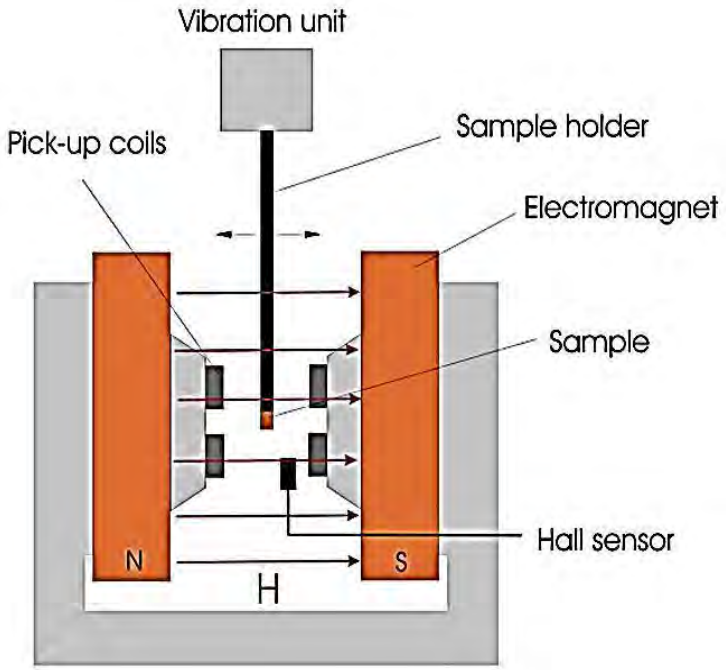

Figure 2.9: Schematic diagram of a vibrating sample magnetometer [83].

3 Chapter 03 Synthesis and Structural Characterizations

In this chapter, synthesis method of cobalt ferrite, P(VDF-TrFE) solution and P(VDF-TrFE) and cobalt ferrite composite solution, films preparation and characterization techniques will be discussed in detail.

3.1 Synthesis of CFO nanoparticles:

CFO nanoparticles can be synthesized by various methods, i-e, sol-gel, wet chemical route [84], co-precipitation [85], precipitation, and heat treatment [86]. Among all these methods, sol-gel is effective, cheap, and less time-consuming. In present study cobalt ferrite nanoparticles (CFO) were synthesized by sol-gel method, which is explained below in detail.

3.1.1 Sol-Gel Method:

Cobalt ferrite (CFO) nanoparticles can be synthesized using different methods. In the present work, the sol-gel process is used because the sol-gel method is very effective, less costly, environment friendly, and easy to produce ceramic powders of high purity, small size, and excellent homogeneity. In the sol-gel process, as the name shows, a solution is prepared, which is transformed into a gel by thermal treatment. The gel is then calcined to remove the organics and obtain the final product. In the present work, Acetic Acid and Ethylene Glycol were used as solvents. A solution of iron nitrate hexahydrate, cobalt nitrate Nano-hydrate, acetic acid, and ethylene glycol was prepared through magnetic stirring. After drying the solution, the gel was grinded in acetone and calcined at 800°C in the furnace. It was observed that the total mass of powder reduced after calcination due to the removal of different compounds.

3.1.2 Precursors:

The chemicals used to synthesize cobalt ferrite (CFO) nanoparticles are listed below:

Table 3.1: Precursors used in the synthesis of CFO nanoparticles.

Chemicals	**Formula**	**Purity**	**Suppliers**	**Molecular Weight**
Cobalt Nitrate Hexahydrate	$Co(NO3)_2 \cdot 6H_2O$	99%	Aladdin® China	291.3 g/mol
Iron Nitrate Nanohydrate	$Fe(NO_3)_2 \cdot 9H_2O$	99.99%	RHAWN™ China	404 g/mol
Acetic Acid	CH_3COOH	99.8%	Chem.-Lab Belgium	60.052 g/mol
Ethylene Glycol	$C_2H_6O_2$	99%	PANREAC QUMICA SA	62.07 g/mol

3.1.3 Synthesis method of CFO nanoparticles:

Stoichiometric quantities of Cobalt Nitrate Hexahydrate [$Co(NO_3)_2 \cdot 6H_2O$] are mixed with the appropriate amount of ethylene glycol [$C_2H_6O_2$] and acetic acid [CH_3COOH] (Solution-1). Similarly, the Stoichiometric amount of iron nitrate Nanohydrate [$Fe(NO_3)_2 \cdot 6H_2O$] is mixed with a suitable amount of ethylene glycol [$C_2H_6O_2$] and acetic acid [CH_3COOH] (Solution-2). Solution-1 and Solution-2 are stirred in a separate beaker for 2 hours without heating. After that, mix Solution-1 and Solution-2 in one cup and go the solution for 4 hours and 30 minutes without heating. Now place this solution on a magnetic stirrer at 60°C for 30 minutes. After that, pour the solution into a Petri dish and cover the Petri dish with aluminum foil. Make small pores on aluminum foil so that evaporation is done easily and steadily. Place the Petri dish in the oven at 80°C for 14 hours. After that, a solid gel appeared. Using mortar and pestle grind the solid gel in acetone for 1 hour. The nano-particles were formed by post-annealing under ambient air conditions in a tube furnace. The size of the nano-particles can be controlled by annealing temperature. I calcined the CFO nanoparticles in a furnace at 800°C for 4 hours. Flow chart of synthesis of CFO nanoparticles is shown in Figure 3.1.

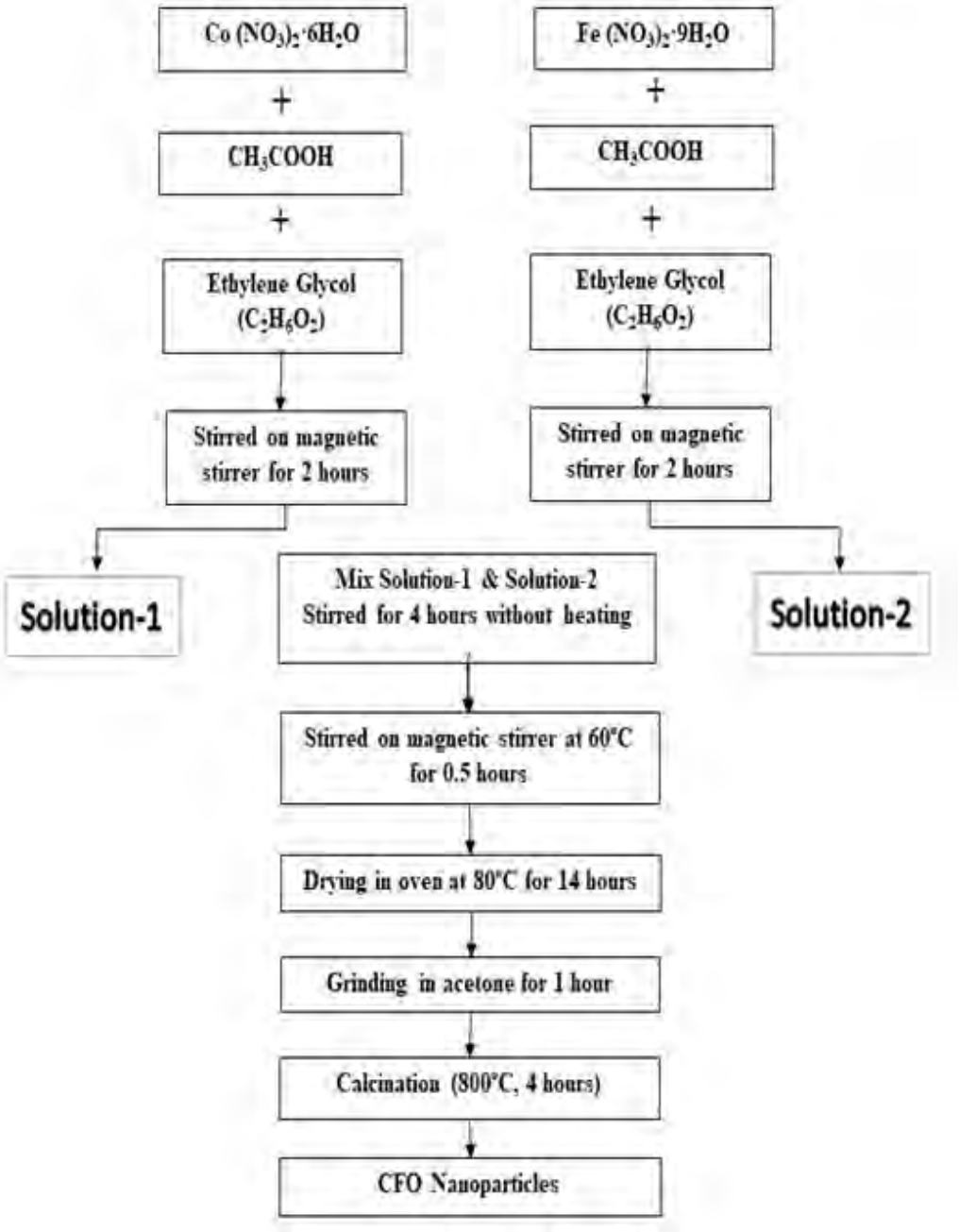

Figure 3.1: Flow chart for the synthesis of cobalt ferrite nanoparticles.

3.2 Synthesis of P (VDF-TrFE) and P(VDF-TrFE)/CFO films:

Different methods can be used to fabricate P(VDF-TrFE) and P(VDF-TrFE)/CFO free-standing films, such as solvent casting spin coating and electrospray deposition (ESD) electrospinning, and spray coating. This work used the solvent casting to synthesize free-standing P(VDF-TrFE) and P(VDF-TrFE)/cobalt ferrite composite films with varying

CFO concentrations. P(VDF-TrFE)/cobalt ferrite composite films containing 05%, 10%, 15%, 20%, 30%, 40%, and 50wt% CFO are named as P(VDF-TrFE)/CFO 95/5, P(VDF-TrFE)/CFO 90/10, P(VDF-TrFE)/CFO 85/15, P(VDF-TrFE)/CFO 80/20, P(VDF-TrFE)/CFO 70/30, P(VDF-TrFE)/CFO 60/40 and P(VDF-TrFE)/CFO 50/50 respectively.

3.2.1 P(VDF-TrFE) Solution Preparation:

P(VDF-TrFE) 15 wt% solution was prepared by dissolving the stoichiometric amount of P(VDF-TrFE) in DMF using magnetic stirrer. The required amount of Dimethyl Formamide (DMF) was first added to the beaker and placed on a heating magnetic stirrer. Following this, the calculated amount of P(VDF-TrFE) for 15 wt% solutions was added to the beaker and allowed to stir for 1 hour at 60°C. After that, solution was stirred on a magnetic stirrer at room temperature for 24 hours to align all the chains of polymer. P(VDF-TrFE) solution preparation flow chart is presented in below Figure 3.2.

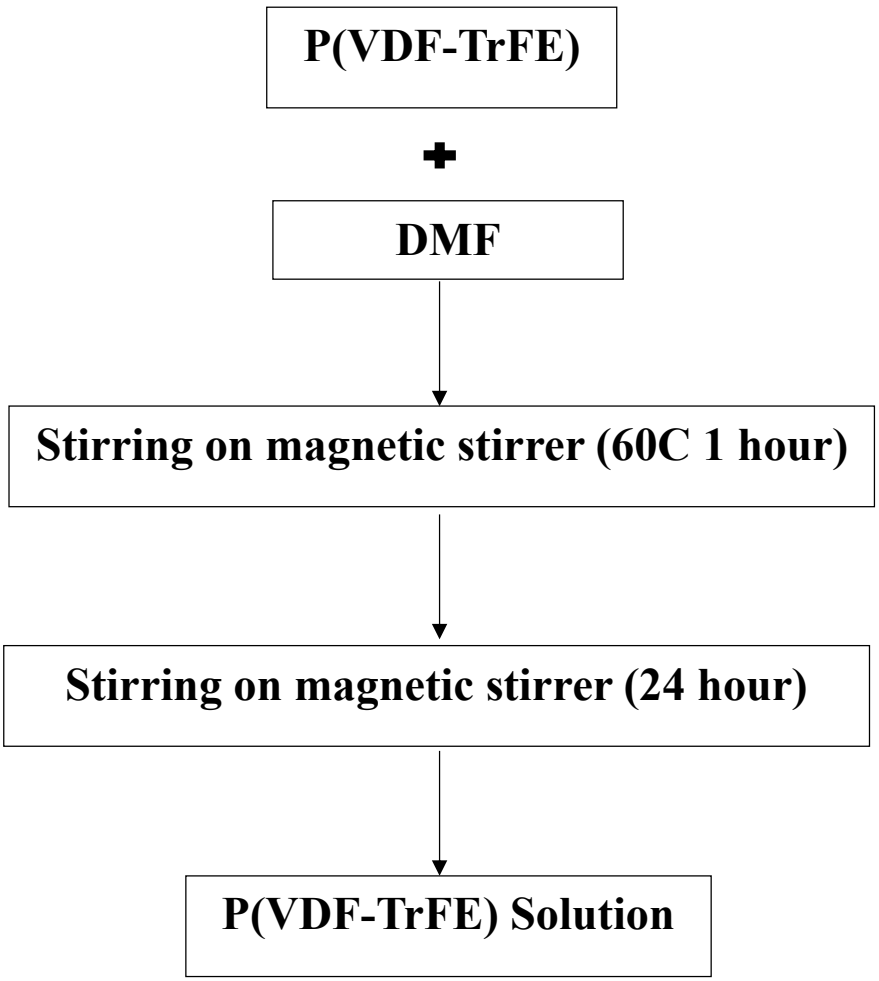

Figure 3.2: Flow chart for the solution preparation of P(VDF –TrFE) Solution.

3.2.2 P(VDF-TrFE)/CFO composite solution Preparation:

To prepare P(VDF-TrFE)/CFO hybrid solution, required amount of cobalt ferrite nanoparticles was dispersed in polymer solution and stirred continuously for 3 hours using an electric motor with a DC power supply having a voltage of 1.8 V and current of 4 A. After 3 hours of stirring, a homogeneous P(VDF-TrFE)/CFO solution was obtained. Seven different solutions containing 05wt%, 10wt%, 15wt%, 20wt%, 30wt% 40wt% and 50wt% CFO concentrations were prepared. Flow chart for the preparation of P(VDF-TrFE)/CFO composite solution is presented in Figure 3.3.

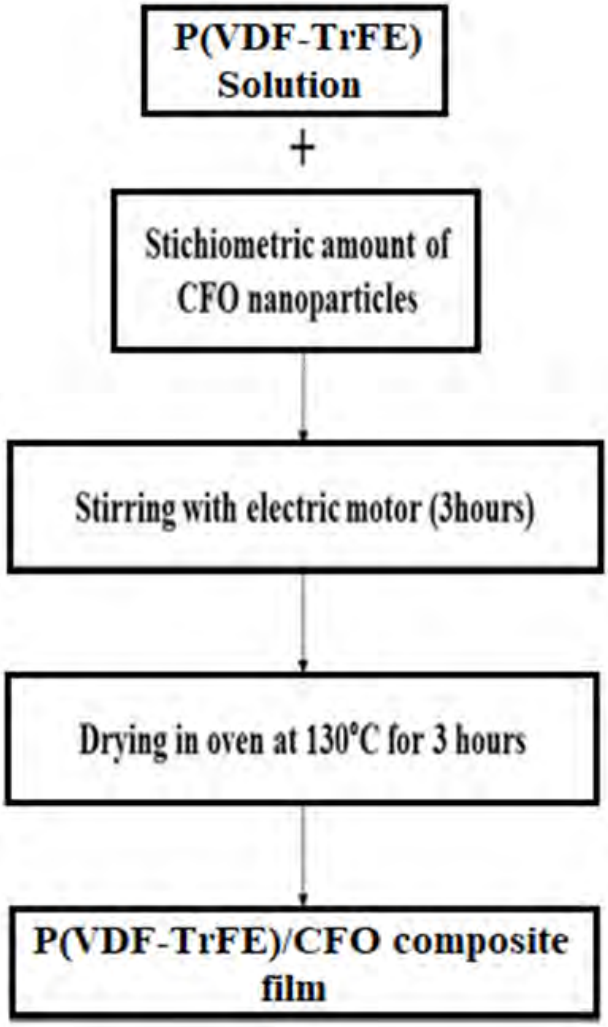

Figure 3.3: Flow chart for the fabrication of P(VDF-TrFE)/CFO composite films.

3.2.3 Film fabrication:

P(VDF-TrFE) and P(VDF-TrFE)/cobalt ferrite free-standing films were prepared using a hand-made 3×1-inch glass cavity. The cavity was filled with the prepared solution

and placed in the oven. For P(VDF-TrFE) copolymer films, evaporation temperature was set at 130°C for 3 hours in the oven. Pristine P(VDF-TrFE) films were prepared using pure P(VDF-TrFE) solutions while P(VDF-TrFE)/cobalt ferrite composite films containing 05wt%, 10wt%, 15wt%, 20wt%, 30wt%, 40wt% and 50wt% CFO were prepared using composite solution. Film fabrication steps of composite films by dry casting method are summarized with the help of flow charts shown in Figures 3.2 and 3.3, respectively. A 3×1 inch film of P(VDF-TrFE)/CFO 85/15 is shown in below Figure 3.4.

Figure 3.4: Glass cavity used for Solvent Casting.

4 Chapter 04 Results and Discussion

4.1 X-Ray Diffraction:

X-ray diffraction technique is used to study the structural characterization of prepared samples. XRD of all the films was done using the PANalytical Empyrean system in the range of 2θ = 10°-80° with 0.02° angle increment and step time of 1 second. XRD patterns of pristine P(VDF-TrFE), Pure CFO, and P(VDF-TrFE)/cobalt ferrite composite films are shown in below Figure 4.1.

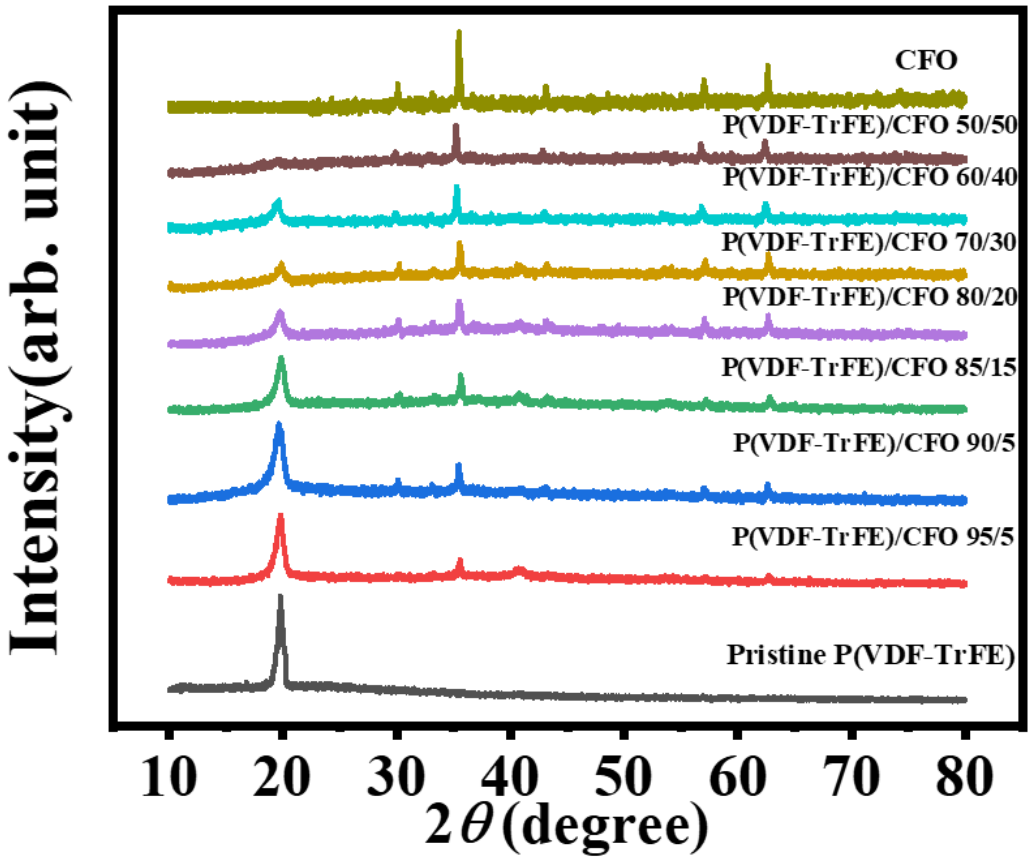

Figure 4.1: XRD pattern of Pristine P(VDF-TrFE), P(VDF-TrFE)/CFO composite films, and pure CFO.

XRD peaks of pure CFO are well match with the reference card PDF # 22-1086, specify the existence of spinel phase of cobalt ferrite [87]. No peaks corresponding to impurity phases are found. Non-appearance of additional diffraction peaks manifest that pure cobalt ferrite nanoparticles were synthesized successfully. Using Scherrer formula, average crystallite size of CFO nanoparticles can be determined.

$$D = \frac{k\lambda}{\beta\cos\theta} \quad (4.1)$$

where "k" is shape factor, "*D*" is crystallite size of particles and its value is 0.91, "β" is full width half maxima (FWHM), "λ" wavelength of X-rays, and "θ" is Bragg's angle [88]. Average crystallite size of CFO nanoparticles calculated from (311) peak is 36.72 nm.

Pristine P(VDF-TrFE) shows highest intensity peak at $2\theta = 19.8^{o}$. This peak corresponds to (110) and (200) planes of β-phase and specify the semicrystalline nature of the polymer [89]. Sharpness of Pristine P(VDF-TrFE) peak shows that there exists only single phase. No phases other than the β-phase is observed in the XRD patterns. P(VDF-TrFE) film is annealed at 130°C to increase the crystallinity of P(VDF-TrFE) [90]. Cobalt ferrite nanoparticles diffraction peaks were present in all composites samples. Presence of ferroelectric β-phase of polymer and CFO nanoparticles was confirmed. XRD peaks of pure CFO are shown in Figure 4.1 as there are multiple peaks of CFO which corresponds to different diffraction planes [57]. There are peaks located at 29.8^{o}, 35^{o}, 42.8^{o}, 56.7^{o} and 62^{o} corresponding to diffraction planes (220), (311), (111), (511) and (440).

In P(VDF-TrFE)/CFO composite films (95/5, 90/10, 85/15), prominent peak related to β-phase is observed, while its intensity reduces in all composite films of P(VDF-TrFE)/CFO. This decrease in peak intensity indicates that concentration of CFO nanoparticles changes the β-phase structure of P(VDF-TrFE). It's due to increase in aggregation of nanoparticles at higher concentrations of CFO, causing non uniform dispersion [91].

With the addition of CFO in all composite films, the peak intensity of CFO increases. Addition of low filler of nanoparticles, induces the crystallization of the β-phase polymer matrix [92]. Also, the peak intensity of P(VDF-TrFE) decreases with the addition of filler concentration. Hence, determining appropriate cobalt ferrite nanoparticle concentration is predominant for elaborating performance of composite films [91].

4.2 Polarization versus electric field response of Pristine P(VDF-TrFE) and P(VDF-TrFE)/CFO composite films:

P-E loops of prepared samples were computed at room temperature, at 10 Hz and 400 Hz frequencies. P-E hysteresis loops of pristine P(VDF-TrFE) is shown in below Figure

4.2. P(VDF-TrFE) showed excellent ferroelectric behavior, which confirms the presence of high concentration of β-phase, as shown by XRD. The addition of TrFE units into PVDF, caused direct crystallization into ferroelectric β-phase.

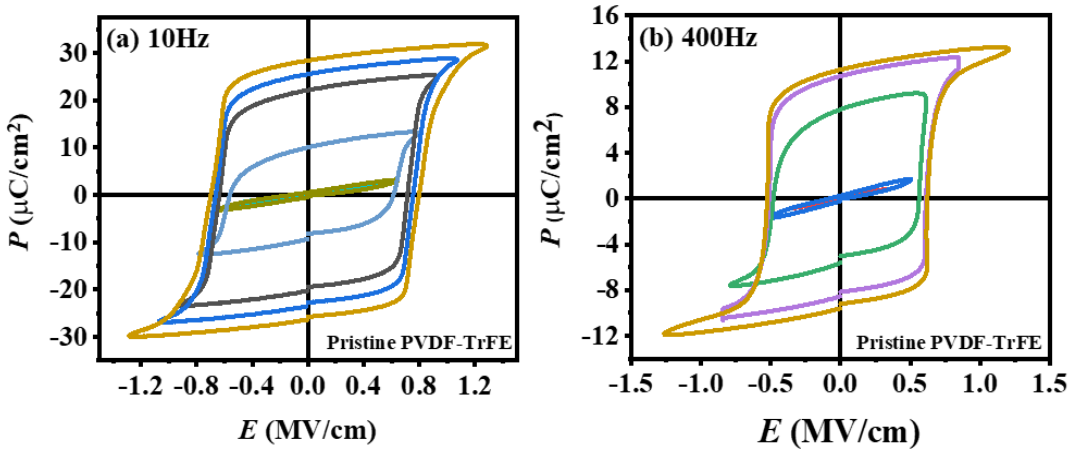

Figure 4.2: P-E loops of pristine P(VDF-TrFE) at (a) 10 Hz and (b) 400 Hz.

For the ferroelectric hysteresis loops measurements Platinum (Pt) electrodes were deposited on thin films by using sputter coater. Ferroelectric hysteresis loops were taken, using standard Sawyer Tower circuit already explained in section 2.2.1. Figure 4.2 shows that PE loops of pristine P(VDF-TrFE) are well saturated.

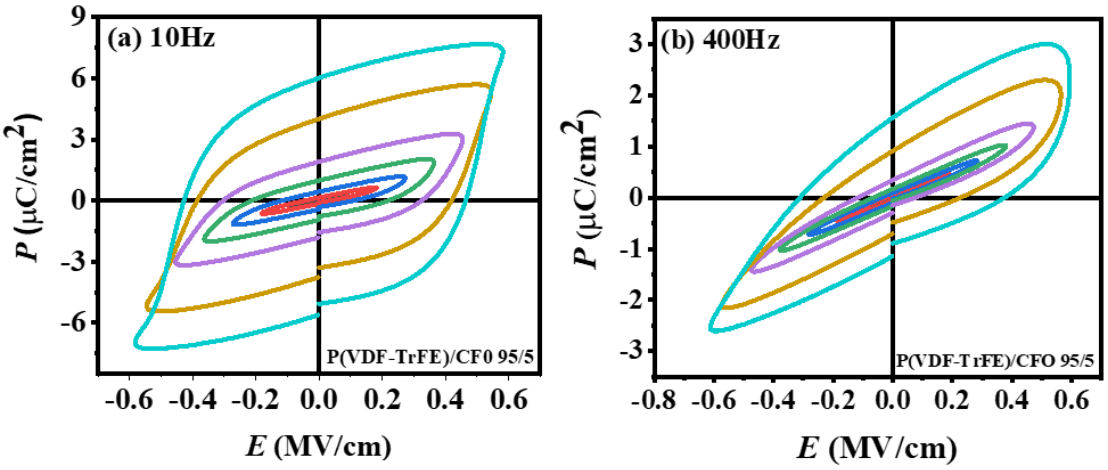

Figure 4.3: P-E loops of (a, b) P(VDF-TrFE)/CFO 95/5.

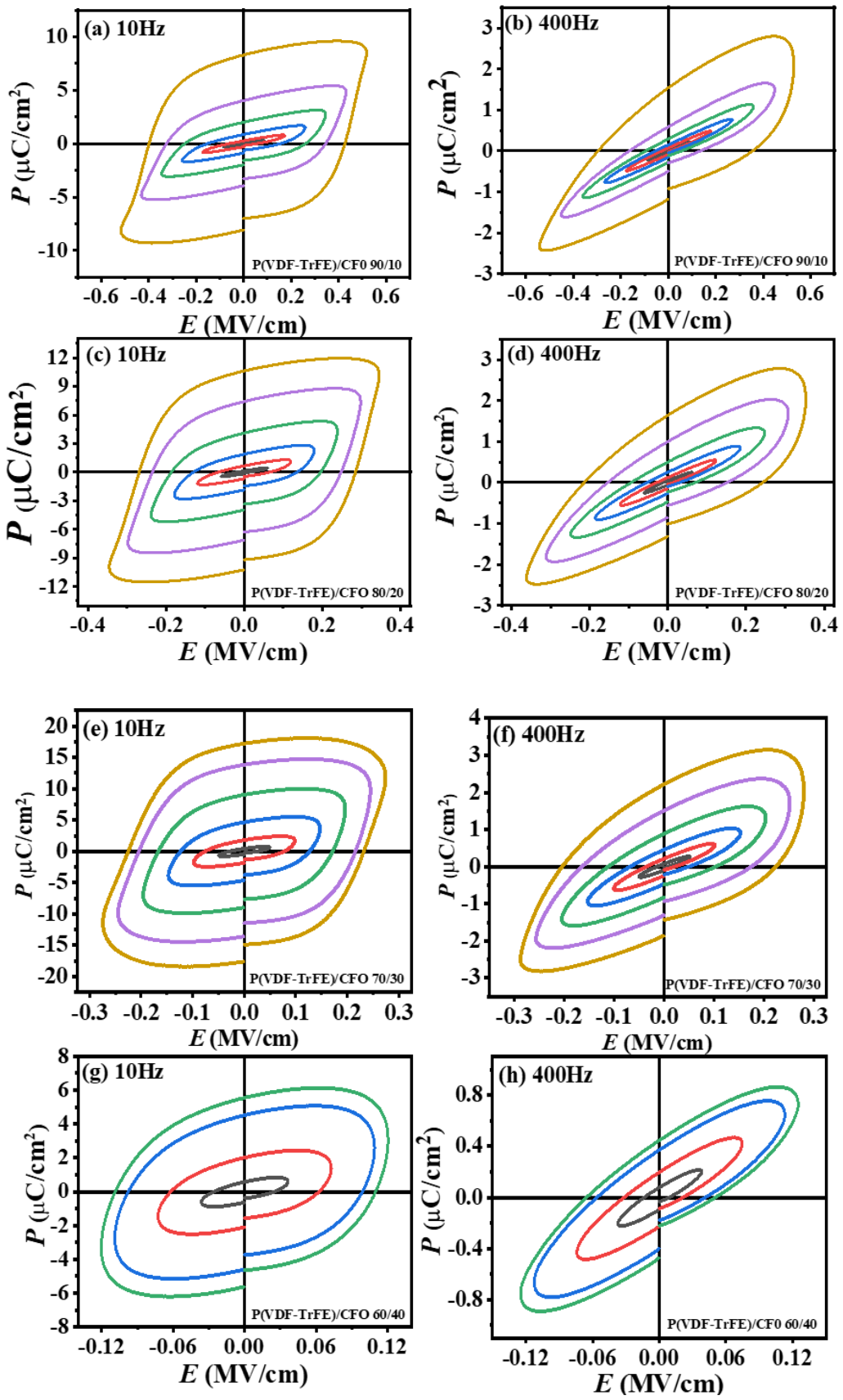

Figure 4.4: P-E loops of (a, b) P(VDF-TrFE)/CFO 90/10,(c, d) P(VDF-TrFE)/CFO 80/20, (e, f) P(VDF-TrFE)/CFO 70/30, (g, h) P(VDF-TrFE)/CFO 60/40.

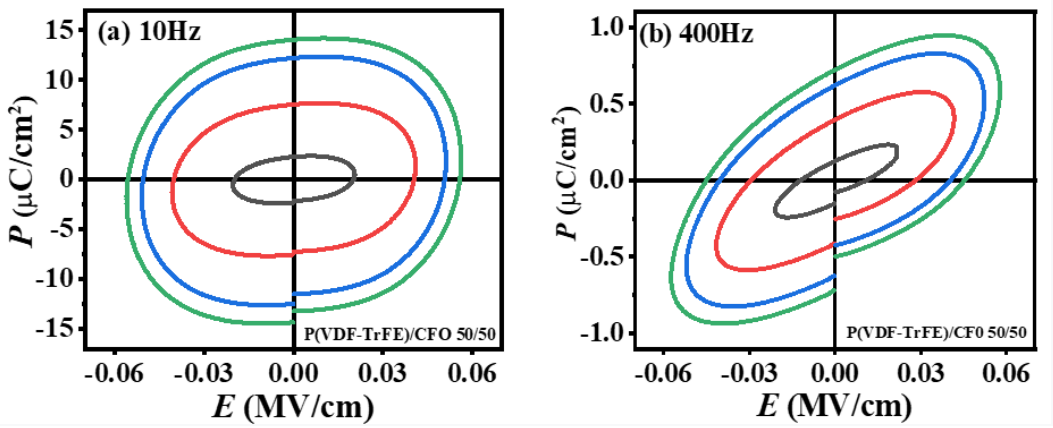

Figure 4.5: P-E loops of (a, b) P(VDF-TrFE)/CFO 50/50.

At room temperature, ferroelectric hysteresis loops of the composite films, with different ferrite weight fractions are presented in Figure 4.3-4.5. P(VDF-TrFE)/CFO 95/5, P(VDF-TrFE)/CFO 90/10, P(VDF-TrFE)/CFO 80/20 and P(VDF-TrFE)/CFO 70/30 samples exhibit saturated hysteresis loops. While P(VDF-TrFE)/CFO 60/40 and P(VDF-TrFE)/CFO 50/50 show lossy capacitor behavior due to the leakage current conduction mechanism. Samples with higher concentration of CFO becomes conducting, indicating the presence of leakage current which have prominent effect on the ferroelectric hysteresis loops. It is reported in literature that this leakage current is the contribution of three current sources:

1) Polarizing current (generated by domain switching).
2) Charging and discharging current (produced due to linear polarization).
3) Leakage current (conductivity of samples) because it is not a perfect insulator[93].

P(VDF-TrFE)/CFO composites also shows decreased breakdown strength as compared to pristine P(VDF-TrFE), due to the additional conduction caused by CFO nanoparticles which facilitates the breakdown mechanism. This phenomenon can be from two reasons. This phenomenon can be from two reasons.

1) Ferrite nanoparticles may instigate additional free charges. These charges are required to compensate and balanced the polarization domain.
2) Ferrite nanoparticles can perform as heterogeneous nucleation centers for ferroelectric domains during the polarization [94, 95].

We notice that coercive field "E_c" is vigorously dependent on the volume proportion of cobalt ferrite nanoparticles [56]. Value of coercive field escalate with the increase in CFO concentration and changes from 0.0094, 0.0155, 0.0514, 0.0810 and 0.0989 MV/cm

under different CFO volume fractions. All these values are measured at 0.11 MV/cm and 10 Hz frequency.

Saturation polarization and remanent polarization increases with the increase in concentration of CFO. Various parameters P_s (saturation polarization), and P_r (remanent polarization) and E_c coercivity is calculated from the obtained P-E loops at 0.11 MV/cm. These parameters are compiled in Table 4.1.

Table 4.1: The P_s, P_r and E_c values at 0.11 MV/cm, ferroelectric hysteresis measurements.

Sample Name	Frequency	P_s (μC/cm^2)	P_r (μC/cm^2)	E_c (MV/cm)
P(VDF-TrFE)/CFO 95/5	10Hz	0.34	0.04	0.0094
	400Hz	0.25	0.02	0.0034
P(VDF-TrFE)/CFO 90/10	10Hz	0.42	0.09	0.0155
	400Hz	0.25	0.035	0.0053
P(VDF-TrFE)/CFO 80/20	10Hz	1.08	0.51	0.0514
	400Hz	0.49	0.10	0.0109
P(VDF-TrFE)/CFO 70/30	10Hz	2.92	2.23	0.0810
	400Hz	0.69	0.25	0.0254
P(VDF-TrFE)/CFO 60/40	10Hz	5.07	4.51	0.0989
	400Hz	0.73	0.35	0.04

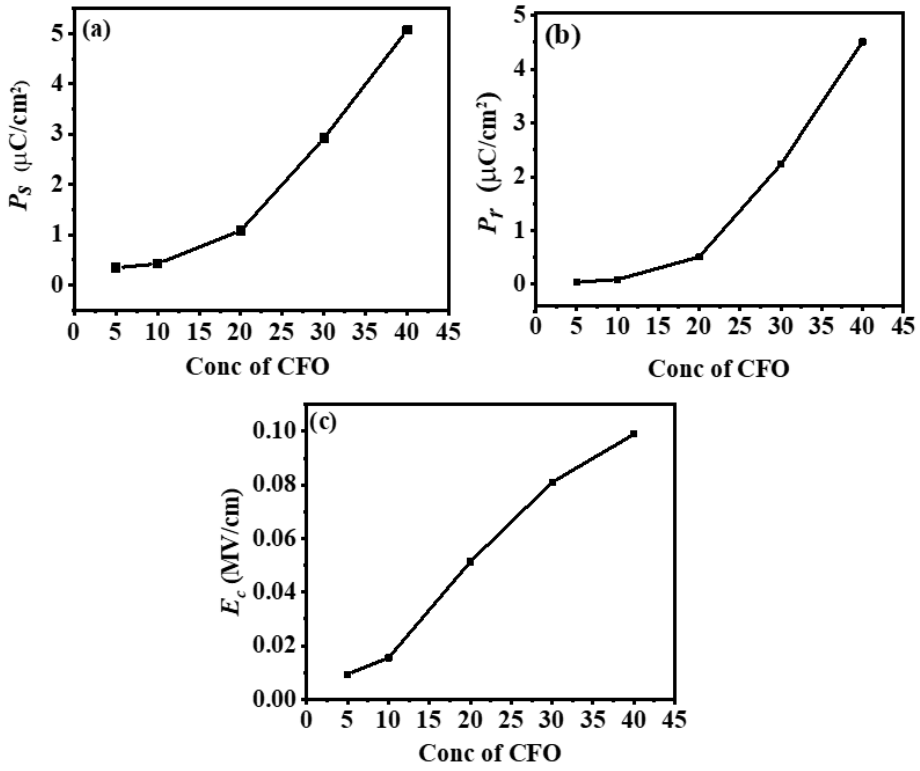

Figure 4.6: Value of P_s, P_r and E_c values plotted against weight fraction of CFO.

At 0.11 MV/cm field and 10 Hz frequency, it is realized that saturation polarization, remanent polarization and coercivity increases as the concentration of CFO increases in P(VDF-TrFE) which is shown in above Figure 4.6 (a-c). Addition of CFO in P(VDF-TrFE) increases the porosity of the system. As a result leakage current of the system increases. This increased leakage current is responsible for the increased value of saturation polarization, coercivity and remanent polarization as a function of CFO concentration in P(VDF-TrFE) prepared films.

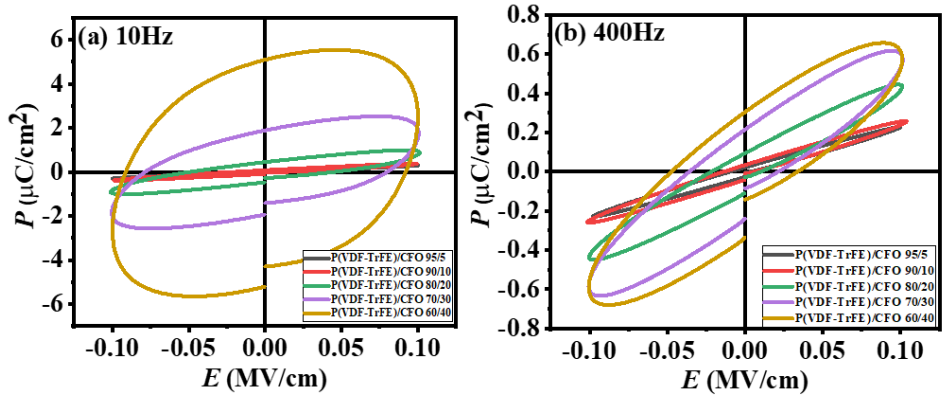

Figure 4.7: Ferroelectric loops of P(VDF-TrFE)/CFO films at maximum electric field of around 0.11 MV/cm.

In above Figure 4.7(a) it is noticed that, as the concentration of CFO increases, hysteresis loops become lossy because of the increase in leakage current in the system. Roundness in the loop is most obvious for P(VDF-TrFE)/CFO 60/40 sample. This is because as the concentration of CFO increases, space charges also increase which contribute to the net polarization of material.

Another important observation is that the area under the loop increases with the addition of CFO. The reason is that with the incorporation of cobalt ferrite nanoparticles, heterogeneous polarization facilitates in the composite film because of the accumulation of charge at interface [96].

4.3 U-Vis Visible Spectroscopy:

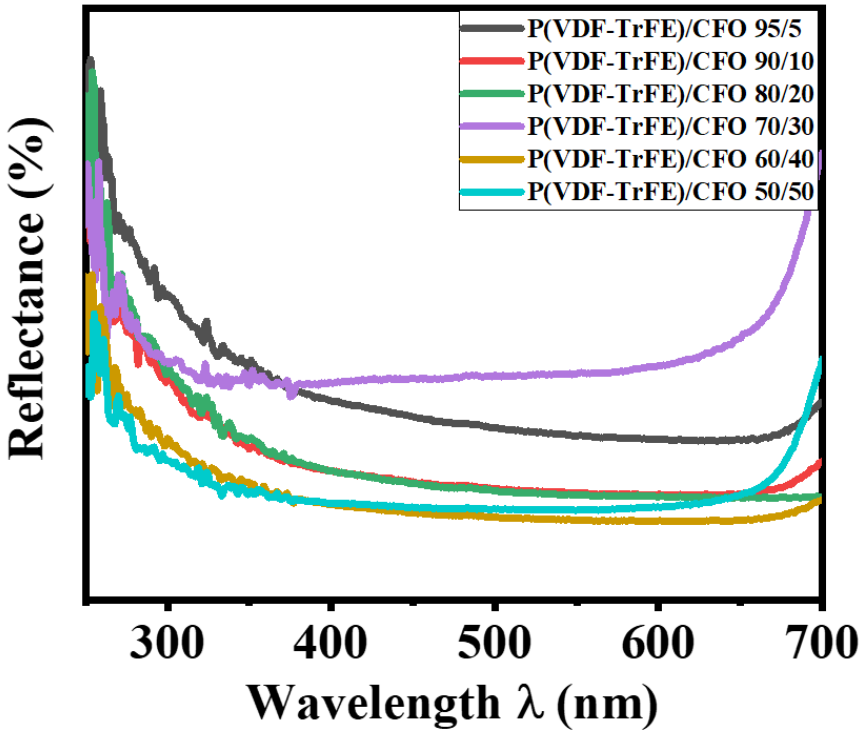

Figure 4.8: Reflectance of P(VDF-TrFE)/CFO composite film.

Reflectance versus wavelength plots of P(VDF-TrFE)/CFO nanocomposites are shown in Figure 4.8. In UV region, as observed in P(VDF-TrFE)/CFO composites reflectance decreases sharply up to about 350 nm, and then decreases linearly until 650 nm. This trend is same in all the composite films. In visible region, no specific trend with the addition of CFO nanoparticles is observed. Figure 4.9 shows the optical absorption spectra of P(VDF-TrFE)/CFO 95/5, P(VDF-TrFE)/ CFO 90/10, P(VDF-TrFE)/CFO 70/30, P(VDF-TrFE)/CFO 60/40 and P(VDF-TrFE)/CFO 50/50 samples.

Direct Bandgap is calculated by plotting $(h\nu*F(R))^2$ versus energy, where $F(R)$ is Kubelka-Munk function:

$$F(R) = \frac{(1-R)^2}{2R} \qquad (4.2)$$

where R is diffuse reflectance. Extrapolating straight line from peak to energy axis gives direct energy bandgap.

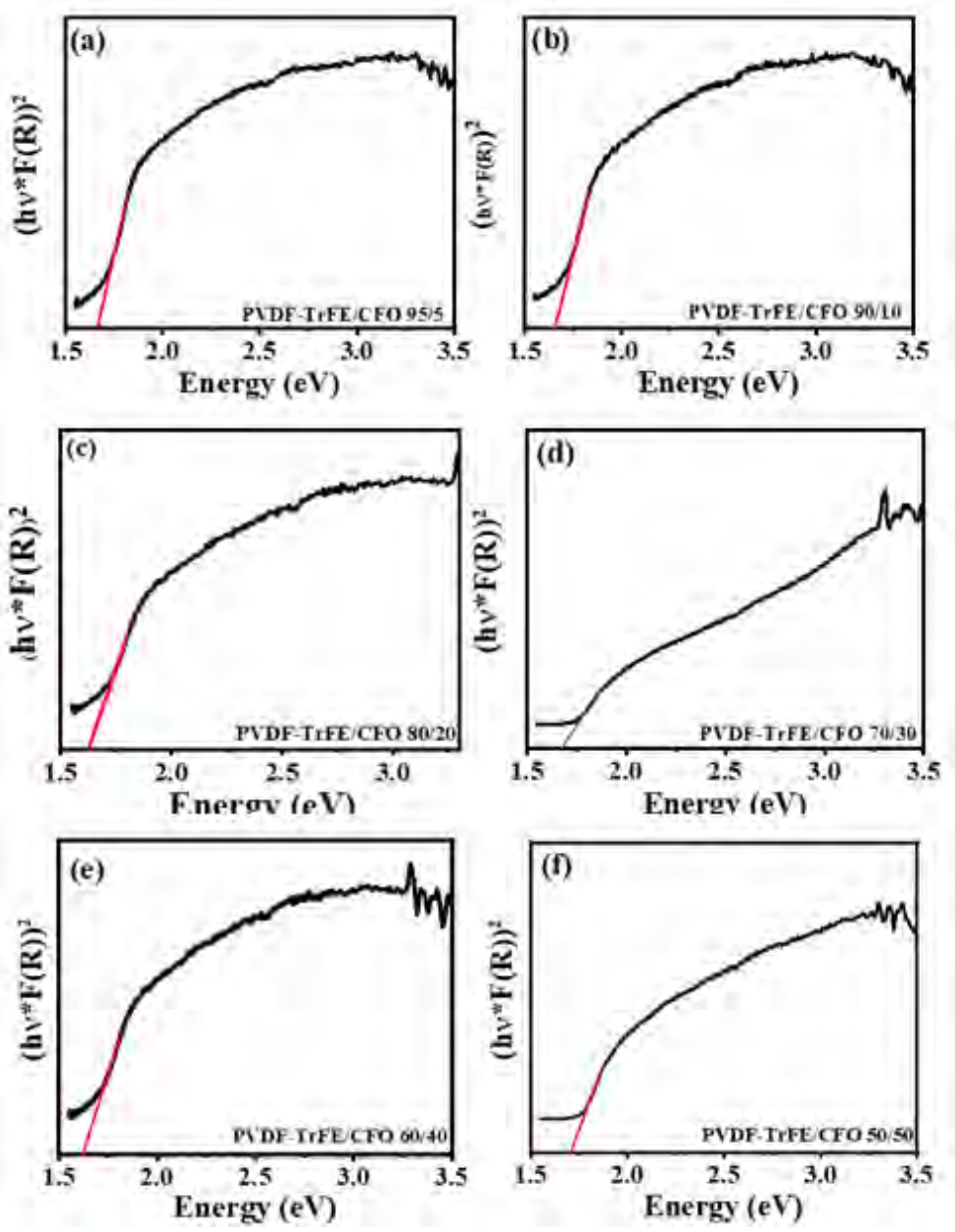

Figure 4.9: $(h\nu*F(R))^2$ versus energy plots for direct band gap of (a) P(VDF-TrFE)/CFO 95/5, (b) P(VDF-TrFE)/CFO 90/10, (c) P(VDF-TrFE)/CFO 80/20, (d)P(VDF-TrFE)/CFO 70/30, (e) P(VDF-TrFE)/CFO 60/40, (f) P(VDF-TrFE)/CFO 50/50.

The bandgap values for P(VDF-TrFE)/CFO 95/5, P(VDF-TrFE)/ CFO 90/10, P(VDF-TrFE)/CFO 80/20, P(VDF-TrFE)/CFO 70/30, P(VDF-TrFE)/CFO 60/40, P(VDF-TrFE)/CFO 50/50 are obtained as 1.66, 1.65, 1.62, 1.67, 1.61 and 1.67 eV respectively. These values are shown in below Table 4.2. No specific trend is observed in the direct energy band gap of prepared films. The optical bandgap in cobalt ferrite is due to *d–d* transitions [97, 98]. Due to the presence of crystal field, level *d* splits into e_g and t_{2g} levels. The energy width between these two levels is different for octahedral and tetrahedral sites. Energy difference relationship for the octahedral sites (Δ_o) and the tetrahedral sites (Δ_t) is given by [99]:

$$\Delta_t = \frac{4}{9}\Delta_o \qquad (4.3)$$

The band gap of $CoFe_2O_4$ nearly equal to 2.2-2.3 eV [100].

Table 4.2: Energy band gap values of P(VDF-TrFE)/CFO samples.

Sample name	Energy band gap (eV)
PVDF-TrFE/CFO 95/5	1.66
PVDF-TrFE/CFO 90/10	1.65
PVDF-TrFE/CFO 80/20	1.62
PVDF-TrFE/CFO 70/30	1.67
PVDF-TrFE/CFO 60/40	1.61
PVDF-TrFE/CFO 50/50	1.67

4.4 FTIR Spectrum of P(VDF-TrFE)/CFO composite films:

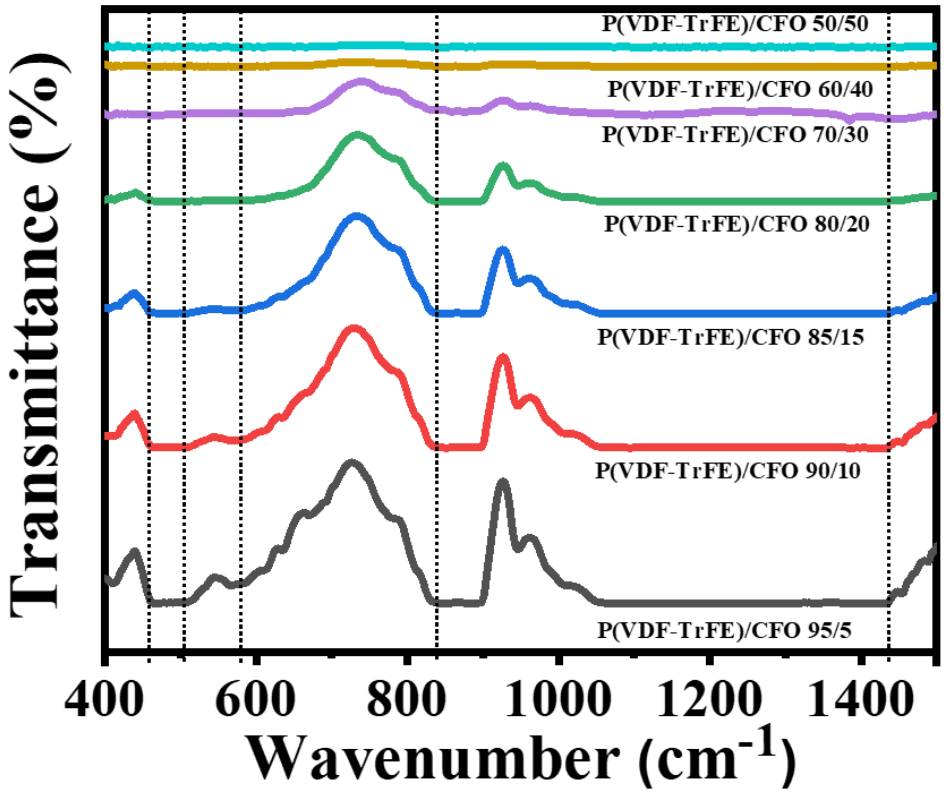

Figure 4.10: FTIR Spectra of P(VDF-TrFE)/CFO composite films.

Fourier-transform infrared spectroscopy (FTIR) allows the existence of different bonds in a crystal. Room temperature FTIR pattern of all prepared samples is shown in Figure 4.10. Most infrared-active vibrations for the copolymer are accumulated in a preferably confined region, 400–1500 cm^{-1} due to large mass of the fluorine atom [101]. Mainly, in spinel ferrites two types of vibration modes are present. Octahedral sites, which appear in the frequency range of 430–370 cm^{-1} and tetrahedral locations, which apparent in the frequency spectrum of 600–500 cm^{-1} [102]. Minor peak observed at 580 cm^{-1} corresponds to characteristic peak of spinel ferrite.

Modes at 661, 504, 841 and 1431 cm^{-1} corresponds to the stretching vibration of the P(VDF-TrFE) polar beta phase [103]. All the modes from 520-580 cm^{-1} are absorption bands which shows the stretching vibration of tetrahedral metal-oxygen bonding, and modes is diminished with the increased of CFO filler content in P(VDF-TrFE). Mode around (578 cm^{-1}) in the tetrahedral site, is ascribed to the stretching vibrations of the Fe^{3+} [tetra] ↔ O bond. Intensity of the mode decreases up to 15wt% CFO sample, after that the mode completely disappeared. Mode observed at 838 cm^{-1} assigned to

the characteristic absorption of the β-phase, which is associated to the mixed CH_2 rocking vibrations and CF_2 asymmetric stretching [104].

The absorption modes, observed at 587–583 cm^{-1} assigned to the tetrahedral complexes also diminishes with the increase of filler content [105]. In all samples with the increase of magnetic nanoparticles CFO, the ferroelectric beta-absorption decreases up to P(VDF-TrFE)/CFO 70/30 and disappeared in sample P(VDF-TrFE)/CFO 60/40 and P(VDF-TrFE)/CFO 50/50. These results are in accordance with the research articles [106].

4.5 M-H and M-T study of P(VDF-TrFE)/CFO composite films:

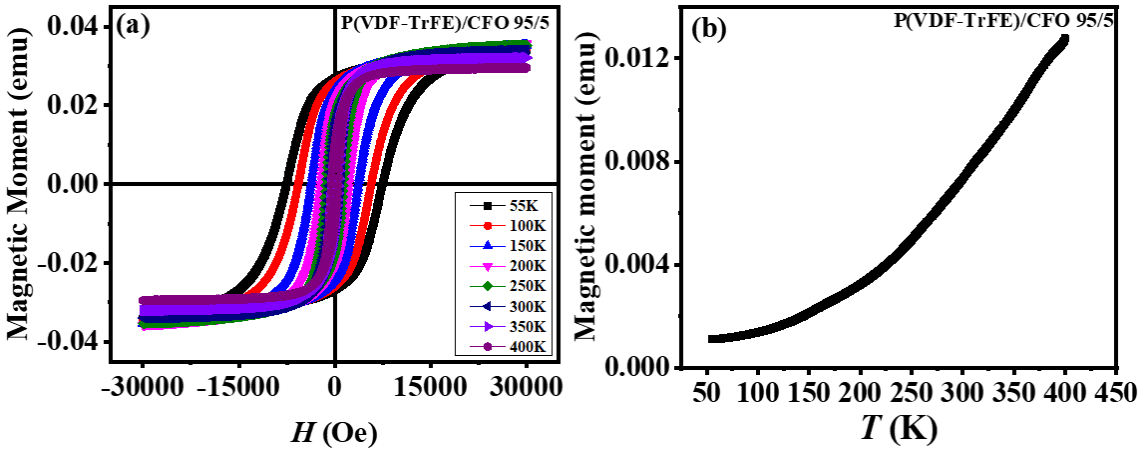

Figure 4.11: (a) M-H and (b) M-T graph of P(VDF-TrFE)/CFO 95/5.

Temperature dependent magnetic measurements were taken for some selected samples at 3 T field. Graph of magnetic moment vs magnetic field of P(VDF-TrFE)/CFO 95/5 in temperature range of (55 K-400 K) is shown in above Figure 4.11(a). The shape and magnetic moment values of the measured magnetic hysteresis loops depict that magnetic particles are arbitrarily oriented within the polymer matrix. Initially by applying external magnetic field magnetic moments aligns themselves and magnetic moment increases until it reaches saturation, where all magnetic moments get align.

All magnetic loops show ferromagnetic behavior and there is increase in the maximum magnetic moment M_s up to 200 K and then there is decrease in the magnetic moment up to 400 K as shown in Figure 4.12(a). The variation of maximum magnetic moment (M_s) values with the increase in temperature is probably due to the rearrangement of cation distribution, i-e., the interchange of Fe^{3+} and Co^{2+} ions from

tetrahedral sites to octahedral sites and vice versa [107]. There is probable two reasons for the decrease of maximum magnetic moment:

1) P(VDF-TrFE) polymer layer can be proposed as a magnetic dead layer because its non-magnetic. Due to this the value of M_r vary, owing that the surface magnetic moment are quenched.
2) Magnetization of the film is interrelated to the volume fraction of CFO nano-particles by: $M_s = \phi_{vn} M_{ns}$, where M_{ns}, is the saturation magnetization of the individual nano- particle and ϕ_{vn} is the volume fraction of the nanoparticles in composite film [108].

The decrease in maximum magnetic moment for temperature range 200- 400 K is based on Bloch's law:

$$M(T) = M(0)\left[1 - \frac{T}{T_0}\right]^{\alpha} \qquad (4.4)$$

where $M(T)$ is temperature dependent magnetization, $\frac{1}{T_0}$ is called the Bloch constant and "α" is Bloch's exponent with a value of 3/2 for bulk materials [109]. Bloch's law is credible for temperature range 200-400 K. At temperatures lower than 200 K, a deviation from the modified Bloch's law occur where a sharp increase in maximum magnetic moment occur for temperature range from 50 K to 199 K [110].

Magnetic moment with respect to temperature is shown in above Figure 4.11(b). Values of magnetic moment continuously increases with the increase in temperature. No evidence of any transition is observed in the measured temperature range.

Table 4.3: The M_s, H_c and M_r values of P(VDF-TrFE)/CFO 95/5.

Temperature (K)	M_s (emu)	H_c (Oe)	M_r (emu)
55	0.0341	7472.7	0.0268
100	0.0347	5695.3	0.0259
150	0.0353	3704.3	0.0241
199	0.0356	2238.8	0.0210

249	0.0353	1377.5	0.0174
299	0.0340	934.7	0.0141
349	0.0321	674.4	0.0116
400	0.0295	521.4	0.0099

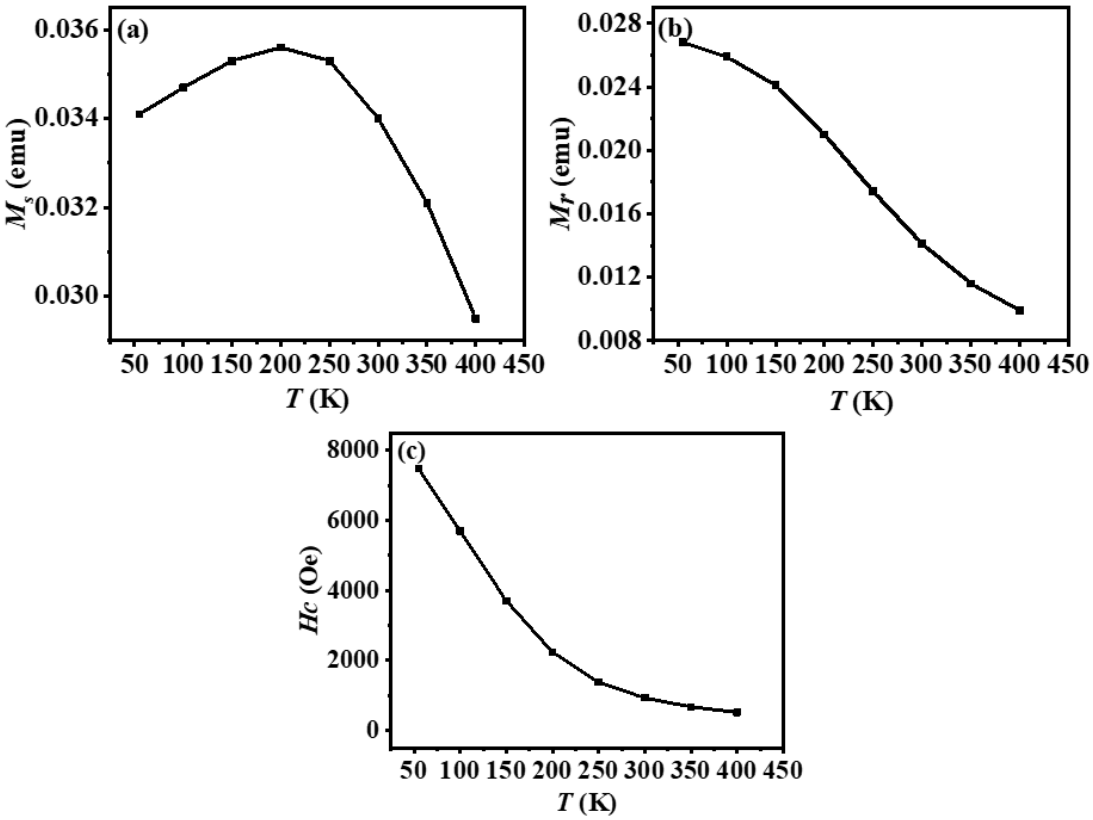

Figure 4.12: (a) M_s (b) M_r and (c) H_c graph of P(VDF-TrFE)/CFO 95/5 as a function of temperature.

Maximum magnetic moment increases with the increase of temperature up to 200 K. After that with the increase in temperature maximum magnetic moment decreases which follow the Bloch's law. Maximum value of magnetic moment is reported as 0.0356 emu at 199 K. At all temperatures, there is continuously decrease in the coercive field and remanent magnetization as observed by above Figure 4.12. Value of coercive field strongly depends on factors such as the size, shape, calcinations temperature and structure of the formed particles [67, 111, 112].

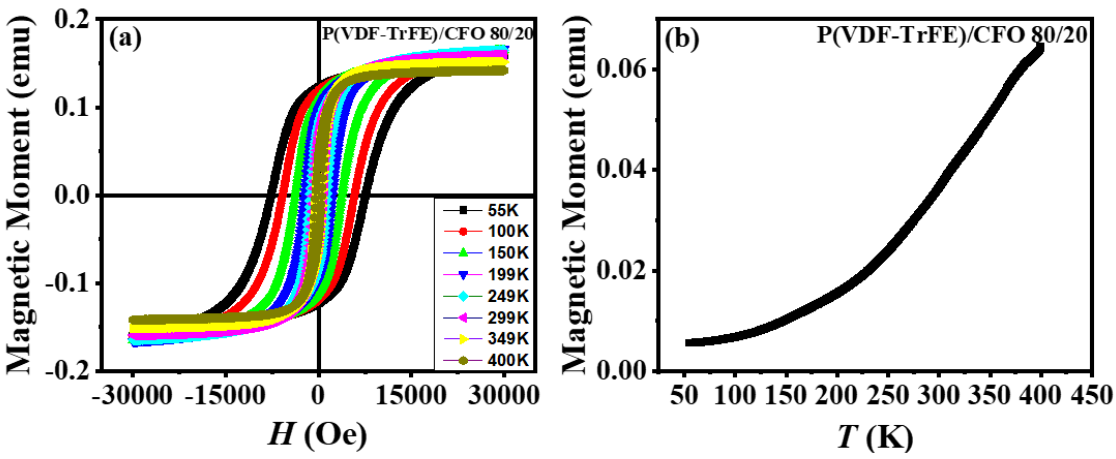

Figure 4.13: (a) M-H and (b) M-T graph of P(VDF-TrFE)/CFO 80/20.

Magnetic moment as a function of applied magnetic field for P(VDF-TrFE) 80/20 sample is shown in Figure 4.13 (a). While magnetic moment with respect to temperature is shown in Figure 4.13 (b). M-H and M-T data follows similar like P(VDF-TrFE)/CFO 95/5 sample. No evidence of any transition is observed in the measured temperature range.

The magnetic moment arises in ferrites due to the uncompensated parallel electron spin of individual ion. Neel's model explained that magnetization intensity is due to metal ion distribution [113]. Neel's model explains that there are three types of interactions A-A, A-B and B-B. The net magnetization is, given by the vector sum of the magnetization of the two sublattices i.e.

$$M_s = M_B - M_A \qquad (4.5)$$

where M_A and M_B are the magnetization of the sub-lattices A and B, respectively.

Some narrow loops are observed with low coercivity values, which confirms the soft ferromagnetic nature of cobalt ferrite [114].

Table 4.4: The M_s, H_c and M_r values of P(VDF-TrFE)/CFO 80/20.

Temperature (K)	M_s (emu)	H_c (Oe)	M_r (emu)
55	0.159	7578.2	0.122
100	0.162	5784.3	0.119
150	0.165	3783.5	0.111
199	0.166	2300.1	0.096
249	0.164	1411.8	0.082
299	0.159	937.5	0.067
349	0.151	670.1	0.055
400	0.141	506.2	0.048

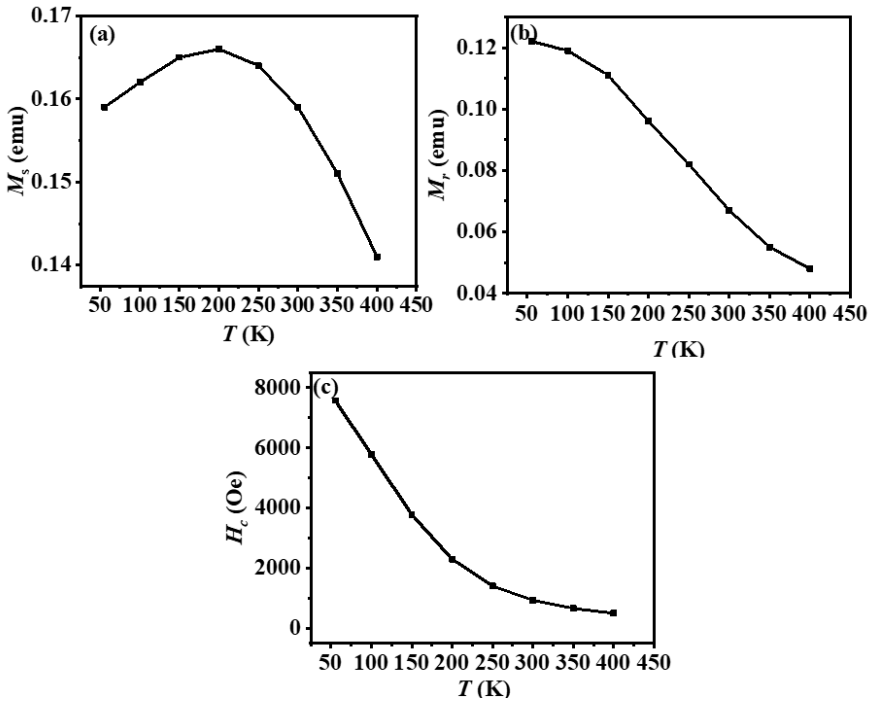

Figure 4.14: (a) M_s (b) M_r and (c) H_c graph of P(VDF-TrFE)/CFO 80/20 as a function of temperature.

Maximum magnetic moment increases with the increase of temperature up to 200 K. After that with the increase in temperature maximum magnetic moment decreases up to 400 K which agrees to Bloch's law. Maximum value of magnetic moment is reported as 0.166 emu at 199 K. Remanent magnetization and coercivity decreases with the increase in temperature as observed by above Figure 4.14.

4.6 Conclusion and summary:

Multiferroics are class of materials where more than one ferroic order is present. In the present work ferromagnetic particles have been incorporated in the ferroelectric polymer which results in formation of a composite. This work mainly focuses on the investigation of structural, magnetic, optical, and ferroelectric properties of polymer nanocomposites with ceramic fillers. These composites are flexible free-standing films. The $CoFe_2O_4$ nanoparticles have been selected as a filler due to their chemical stability, mechanical hardness, high saturation magnetization, coercivity and high electromagnetic performance. While PVDF-TrFE is selected as polymer matrix due to their good mechanical flexibility, ferroelectric properties, and good breakdown strength. $CoFe_2O_4$ nanoparticles were prepared by sol-gel method. XRD pattern of $CoFe_2O_4$ nanoparticles confirms its cubic spinel structure. XRD pattern of PVDF-TrFE/$CoFe_2O_4$ composite films, showed that addition of $CoFe_2O_4$ nanoparticles decreases the content of β-phase and crystallinity of PVDF-TrFE matrix.

Ferroelectric loop measurements of PVDF-TrFE/$CoFe_2O_4$ films showed good ferroelectric loops at low concentration of $CoFe_2O_4$ fillers which confirms that $CoFe_2O_4$ nanoparticles are well dispersed in polymer matrix and confirms that addition of TrFE units resulted in a high content of β-phase, which was also confirmed by XRD. While at high concentration of filler content rounded loops appeared (above 30wt%) because conductivity arises due to the additional free charges of $CoFe_2O_4$. PVDF-TrFE/$CoFe_2O_4$ composite films with different $CoFe_2O_4$ content compared at 0.11 MV/cm have showed that increasing the content of $CoFe_2O_4$ filler increases the value polarization at given field due to the contribution of leakage current and interfacial polarization. Decrease in β-phase content with the increase of filler was also confirmed by P-E loop measurements. Another important observation was decrease in the breakdown electric field of composite films with the increase in $CoFe_2O_4$ content.

UV-Visible spectroscopy was performed in the wavelength range of 250-700 nm. Reflectance and bandgap spectra of all composite films exhibited almost similar behavior. The

$(h\nu*F(R))^2$ versus energy plots of all composite films showed hump of $CoFe_2O_4$ phases. FTIR analysis shows that modes associated with the β-phase is observed at specific wavenumbers. Spinel ferrites have two types of vibration modes; tetrahedral sites, which indicate in the frequency range of 600–500 cm^{-1}, and octahedral sites, which appear in the frequency range of 430–370 cm^{-1}. No modes of alpha phase are observed which is consistent with the XRD results.

Temperature dependent M-H study reveals the saturated ferromagnetic hysteresis loops. The shape of hysteresis loops changes with increase in temperature due to the presence of the thermal fluctuations. Both temperature dependent magnetization and hysteresis behavior have been presented. Remanent magnetization and coercive field decrease with the increase in temperature. Data has been analyzed on the bases of Bloch's law.

References:

1. J. W. Nicholson, " *History of polymer systems*" Educ. Chem. **28**, 1991: p. 70.
2. Wahby, W.J.S.P., *Fifty Years' History of Polymers in Concrete in Review.* 2003. **214**: p. 13-22.
3. Morgan, P.W., *Brief History of Fibers from Synthetic Polymers.* Journal of Macromolecular Science: Part A - Chemistry, 1981. **15**(6): p. 1113-1131.
4. Coelho, R., *Physics of Dielectrics for the Engineer*. Vol. 1. 1979: Elsevier.
5. Singh, A. and C. Kumari, *Frequency Dependent Dielectric Study of Aqueous Electrolytes*. 2018.
6. Muhammad Taha Jilani, M.Z.u.R., Abid Muhammad Khan, and S.M.A. Muhammad Talha Khan, *A Brief Review of Measuring Techniques for Characterization of Dielectric Materials.* ITEE Journal, December 2012 **1**: p. 1-2.
7. Mao, S., *Capacitor Fundamentals – Dielectric Polarization.* Apr 23, 2019. **Part 4**.
8. Kao, K.C., *Electric Polarization and Relaxation.* Science Direct, 2004: p. 1.
9. Wördenweber, R., *Ferroelectric Thin Layers, Comprehensive Semiconductor Science and Technology.* Elsevier, Amsterdam, 2011: p. 06.
10. Chi, K., *Electric Polarization And Relaxation.* Science Direct, 2004: p. 2.
11. Kao, K.C., *Dielectric phenomena in solids. .* Academic press, 2004. **17**: p. 433-456.
12. Pettinelli, E., et al., *Dielectric Properties of Jovian Satellite Ice Analogs for Subsurface Radar Exploration: A Review: Jovian Icy Moons Dielectric Properties.* Reviews of Geophysics, 2015. **53**.
13. Badr, A.M., H.A. Elshaikh, and I.M. Ashraf, *Impacts of Temperature and Frequency on the Dielectric Properties for Insight into the Nature of the Charge Transports in the Tl2S Layered Single Crystals %J Journal of Modern Physics.* 2011. **Vol.02No.01**: p. 14.
14. Cambridge, U.o., *Effect of structure on the dielectric constant.* Dissemination of IT for the Promotion of Materials Science (DoITPoMS): p. 1.
15. Graça, M., et al., *Electrical, dielectric and structural properties of borovanadate glass systems doped with samarium oxide.* 2011. **8**(11-12): p. 3107-3110.
16. Sharma, S., V. Renu, and N. Kumar, *Effect of Electric Field and Temperature on Dielectric Constant and Piezoelectric Coefficient of Piezoelectric Materials: A Review.* Integrated Ferroelectrics, 2015. **167**: p. 154-175.
17. El Khaled, D., et al., *Dielectric spectroscopy in biomaterials: Agrophysics.* 2016. **9**(5): p. 310.
18. Jadhav, V.V., R.S. Mane, and P.V. Shinde, *Basics of Ferrites: Structures and Properties*, in *Bismuth-Ferrite-Based Electrochemical Supercapacitors*. 2020, Springer. p. 37-45.

19. Rashdan, S.A., L.J.J.A.J.o.B. Hazeem, and A. Sciences, *Synthesis of spinel ferrites nanoparticles and investigating their effect on the growth of microalgae Picochlorum sp.* 2020. **27**(1): p. 134-141.

20. McClure, D.S.J.J.o.P. and C.o. Solids, *The distribution of transition metal cations in spinels.* 1957. **3**(3-4): p. 311-317.

21. Trivedi, S., et al., *Current scenario of CNG vehicular pollution and their possible abatement technologies: an overview.* 2020. **27**(32): p. 39977-40000.

22. Willard, M.A., et al., *Magnetic properties of ordered and disordered spinel-phase ferrimagnets.* 1999. **82**(12): p. 3342-3346.

23. García-Muñoz, P., et al., *Ferrite Materials for Photoassisted Environmental and Solar Fuels Applications.* Topics in Current Chemistry, 2019. **378**: p. 6.

24. Zhang, Z.J., et al., *Temperature dependence of cation distribution and oxidation state in magnetic Mn− Fe ferrite nanocrystals.* 1998. **120**(8): p. 1800-1804.

25. Silveyra, J.M., et al., *Soft magnetic materials for a sustainable and electrified world.* 2018. **362**(6413): p. eaao0195.

26. Mathew, D.S. and R.-S.J.C.e.j. Juang, *An overview of the structure and magnetism of spinel ferrite nanoparticles and their synthesis in microemulsions.* 2007. **129**(1-3): p. 51-65.

27. Strnat, K.J.J.P.o.t.I., *Modern permanent magnets for applications in electro-technology.* 1990. **78**(6): p. 923-946.

28. Vedrtnam, A., et al., *A comprehensive study on structure, properties, synthesis and characterization of ferrites.* 2020. **7**(6): p. 800-835.

29. Roberts, S.J.P.R., *Dielectric and piezoelectric properties of barium titanate.* 1947. **71**(12): p. 890.

30. Wu, F.J.P.R.L., *Exactly soluble model of the ferroelectric phase transition in two dimensions.* 1967. **18**(15): p. 605.

31. Wang, W., et al., *Advancing versatile ferroelectric materials toward biomedical applications.* 2021. **8**(1): p. 2003074.

32. Pradhan, S. and G.J.R. Roy, *Study the crystal structure and phase transition o f BaTiO 3–A pervoskite.* 2013. **5**(3): p. 63-67.

33. Sharifi Dehsari, H., *Towards multi-ferroic nanocomposites from ferroelectric polymer and magnetic nanoparticles*. 2019, Johannes Gutenberg-Universität Mainz.

34. Vendik, O. and S.J.J.o.A.P. Zubko, *Ferroelectric phase transition and maximum dielectric permittivity of displacement type ferroelectrics (Ba x Sr 1− x TiO 3).* 2000. **88**(9): p. 5343-5350.

35. Xia, W. and Z. Zhang, *PVDF-based dielectric polymers and their applications in electronic materials.* IET Nanodielectrics, 2018. **1**.

36. Ma, Z., et al., *Modeling of hysteresis loop and its applications in ferroelectric materials.* 2018. **44**(4): p. 4338-4343.

37. Lone, D.I., et al., *Multiferroic ABO3 Transition Metal Oxides: a Rare Interaction of Ferroelectricity and Magnetism.* Nanoscale Research Letters, 2019. **14**.

38. Li, G.R., N. Kagami, and H.J.J.o.a.p. Ohigashi, *The possibility of formation of large ferroelectric domains in a copolymer of vinylidene fluoride and trifluoroethylene.* 1992. **72**(3): p. 1056-1061.

39. Chen, X.-Z., et al., *A polymer blend approach to tailor the ferroelectric responses in P (VDF–TrFE) based copolymers.* 2013. **54**(9): p. 2373-2381.

40. Gil, H.A., et al., *Structural modifications of vinylidene fluoride-trifluoroethylene (70-30) copolymer induced by X-ray irradiation.* 1998. **61**(2): p. 265-273.

41. Fujisaki, Y., *"Poly (vinylidenefluoride-trifluoroethylene) P (VDF-TrFE)/semiconductor structure ferroelectric-gate FETs"*, in *Ferroelectric-Gate Field Effect Transistor Memories*. 2016, Springer. p. 157-183.

42. Branciforti, M.C., et al., *New technique of processing highly oriented poly (vinylidene fluoride) films exclusively in the β phase.* 2007. **45**(19): p. 2793-2801.

43. Meng, N., et al., *Nanoscale interfacial electroactivity in PVDF/PVDF-TrFE blended films with enhanced dielectric and ferroelectric properties.* 2017. **5**(13): p. 3296-3305.

44. Hasegawa, R., et al., *Crystal structures of three crystalline forms of poly (vinylidene fluoride).* 1972. **3**(5): p. 600-610.

45. Salimi, A. and A.J.P.T. Yousefi, *Analysis method: FTIR studies of β-phase crystal formation in stretched PVDF films.* 2003. **22**(6): p. 699-704.

46. Shi, F., et al., *Preparation and characterization of PVDF/TiO2 hybrid membranes with different dosage of nano-TiO2.* 2012. **389**: p. 522-531.

47. Arshad, A.N., et al., *Dielectric and Structural Properties of Poly(vinylidene fluoride) (PVDF) and Poly(vinylidene fluoride-trifluoroethylene) (PVDF-TrFE) Filled with Magnesium Oxide Nanofillers.* Journal of Nanomaterials, 2019. **2019**: p. 5961563.

48. Hosni, N., et al., *Semi-hard magnetic properties of nanoparticles of cobalt ferrite synthesized by the co-precipitation process.* Journal of Alloys and Compounds, 2017. **694**: p. 1295-1301.

49. Manzak, A. and Y. Yildiz, *Introductory Chapter: Cobalt Compounds and Applications*, in *Cobalt Compounds and Applications*. 2019, IntechOpen.

50. Mohammad, A., et al., *STRUCTURAL AND MAGNETIC PROPERTIES OF Mg-Co FERRITE NANOPARTICLES.* 2018. **13**(3).

51. Cunningham, K.M., *Reconstructing Ancient "Cobalt Blue" Technology from an Experimental and Theoretical Approach*. 2019: University of California, Los Angeles.

52. Zeng, X., et al., *Direct observation of cation distributions of ideal inverse spinel CoFe2O4 nanofibres and correlated magnetic properties.* Nanoscale, 2017. **9**.

53. Bozorth, R., E.F. Tilden, and A.J.J.P.R. Williams,, *Anisotropy and magnetostriction of some ferrites.* 1955. **99(6)**: p. p. 1788.

54. Fritsch, D.a.C.J.P.R.B.E., *First-principles calculation of magnetoelastic coefficients and magnetostriction in the spinel ferrites CoFe 2 O 4 and NiFe 2 O 4.* 2012. **86(1):**: p. p. 014406.

55. Supriya, S., L. Kumar, and M.J.P.C. Kar, *Optimization of dielectric properties of PVDF–CFO nanocomposites.* 2019. **40**(3): p. 1239-1250.

56. Zhang, J., et al., *The effect of magnetic nanoparticles on the morphology, ferroelectric, and magnetoelectric behaviors of CFO/P (VDF-TrFE) 0–3 nanocomposites.* 2009. **105**(5): p. 054102.

57. Mu, X., et al., *Poly (vinylidene fluoride-trifluoroethylene)/cobalt ferrite composite films with a self-biased magnetoelectric effect for flexible AC magnetic sensors.* 2021. **56**(16): p. 9728-9740.

58. Mu, X., et al., *Poly(vinylidene fluoride-trifluoroethylene)/cobalt ferrite composite films with a self-biased magnetoelectric effect for flexible AC magnetic sensors.* Journal of Materials Science, 2021. **56**(16): p. 9728-9740.

59. Rollik D, B.S.a.G.-M.R., *Separate contributions to the pyroelectricity in poly(vinylidene fluoride) from the amorphous and crystalline phases, as well as from their interface.* J. Appl. Phys. 85 3282–8.

60. KusumaDY, N.L.P.S., *Enhanced ferroelectric switching characteristics of P(Vdf-Trfe) for organic memory devices.* J. Phys. Chem. B 114 13289–93.

61. Guo Y, L.Y., Wang J, Withers R L, Chen H, Jin L and Smith, *Giant magnetodielectric effect in 0−3 Ni0.5zn0.5fe2o4-Poly(vinylidene-fluoride) nanocomposite films.* The Journal of Physical Chemistry C **114, 32**.

62. Prabhakaran, T. and J.J.C.I. Hemalatha, *Combustion synthesis and characterization of cobalt ferrite nanoparticles.* 2016. **42**(12): p. 14113-14120.

63. Hari, M.A., et al., *Performance Enhancement of Flexible and Self-Powered PVDF-ZnO Based Tactile Sensors.* 2022. **22**(10): p. 9336-9343.

64. P Martins1, A.L., J Gutierrez2, J M Barandiaran2, I Orue3 and and S. Lanceros-Mendez1, *Optimizing piezoelectric and magnetoelectric responses on CoFe2O4/P(VDF-TrFE) nanocomposites.* J. Phys. D: Appl. Phys. 44 (2011) 495303 (7pp).

65. Elina Manova, B.K., Daniela Paneva, Ivan Mitov, Lachezar Petrov, Claude Estournès, Céline D'Orléan, Jean-Luc Rehspringer, and Mohamedally Kurmoo, *Mechano-Synthesis, Characterization, and Magnetic Properties of Nanoparticles of Cobalt Ferrite, CoFe2O4.* Chem. Mater., 2004. **16, 26**: p. 5689–5696.

66. GaoLinYan, Y.Z.D.L.L.R.J., *Composition and magnetic properties of cobalt ferrite nano-particles prepared by the co-precipitation method.* J. Appl. Phys. 99, 08G702, 2010. **322**: p. 3470-3475.

67. Martins P, L.A., Gutiérrez J, Barandiarán JM, Orue I and Lanceros-Méndez S 2011, *Optimizing piezoelectric and magnetoelectric responses on Cofe2o4/P (Vdf-Trfe) nanocomposites.* J. Phys.D44 495303.

68. Adhikary P, G.S.a.M., *The Co-operative performance of a hydrated salt assisted sponge like P (Vdf-Hfp) piezoelectric generator: an effective piezoelectric based energy harvester.* Phys. Chem. Chem. Phys. 17 7275–81, 2015.

69. Weimin Xia, Y.Y., Zhicheng Zhang, et al., *The magnetoelectric effect of the CFO thin film by coupling a P(VDF-co-TrFE) piezoelectric layer.* J. Appl. Phys. , 2018. **124.15**.

70. C.-W. Nan, N.C., L. Liu, J. Zhai, Y. Ye, and Y. Lin, *Coupled magnetic-electric properties and critical behavior in multiferroic particulate composites;.* J. Appl. Phys. 124, 154102 (2018);, 2003;. **94**.

71. K. Zhao, K.C., Y. R. Dai, J. G. Wan, and J. S. Zhu, *Effect of martensitic transformation on magnetoelectric properties of Ni2MnGa/PbZr0.52Ti0.48O3 composite.* Appl. Phys. Lett. 162901, 2005;. **87 .16**.

72. Ce-Wen Nan, M.I.B., Shuxiang Dong, et al, *Multiferroic magnetoelectric composites: historical perspective, status, and future directions.* J. Appl.Phys. 031101, 2008;. **103**.

73. Liu, M., et al.,, *Preparation, structure and thermal properties of polylactide/sepiolite nanocomposites with and without organic modifiers.* 2012. **72(13):**: p. p. 1508-1514.

74. Zhou, T., et al.,, *Improving dielectric properties of BaTiO3/ferroelectric polymer composites by employing surface hydroxylated BaTiO3 nanoparticles.* 2011,. **3(7):**: p. p. 2184-2188.

75. F, L.J., *"Structure and ferroelectric properties of P(VDF-TRFE) copolymers"* Ferroelectrics, 1989. **91.1**: p. 303-17.

76. Sencadas V, L.-M.S.a.M.J.F., *Behaviour of the ferroelectric phase transition of P(VDF/TrFE) (75/25) with increasing deformation;.* Ferroelectrics, 2004;. **304 853–6**.

77. Fujisaki, Y.J.F.-G.F.E.T.M., *Poly (Vinylidenefluoride-trifluoroethylene) P (VDF-TRFE)/semiconductor structure ferroelectric-gate FETs.* 2016,: p. p. 157-183.

78. A.H. Compton and S.K. Allison, *"A quantum theory of the scattering X-Rays by light elements".* Physical reveiw,, 1923. **21(5)**: p. 483.

79. Mukherjee, D., *Growth and characterization of epitaxial thin films and multiferroic heterostructures of ferromagnetic and ferroelectric materials.* 2010.

80. Trout, S.R., *Magnetic Testing of Bonded Magnets.* Springer, Dordrecht, (2003). **118**.

81. Sutton, M.A., et al.,, *Scanning electron microscopy for quantitative small and large deformation measurements part I: SEM imaging at magnifications from 200 to 10,000.* 2007. **47(6):**: p. p. 775-787.

82. Rafique, M., *Study of the Magnetoelectric Properties of Multiferroic Thin Films and Composites for Device Applications.* Diss. COMSATS Institute of Information Technology Lahore Campus-Pakistan., 2015.

83. Dawber, M., K. Rabe, and J.J.R.o.m.p. Scott,, *Physics of thin-film ferroelectric oxides.* 2005. **77(4):**: p. p. 1083.

84. Siva, K.V., et al., *Structural, magnetic and magnetoelectric investigations on CoFe2O4 prepared via various wet chemical synthesis route: A Comparative Study.* 2021. **535**: p. 168065.

85. Huang, S., et al., *Photo-electrochemical and photocatalytic properties of hierarchical flower-like BiOI/CoFe2O4 nanocomposites synthesized by co-precipitation method.* 2021. **111**: p. 110643.

86. Rodríguez-Rodríguez, A.A., et al., *Spinel-type ferrite nanoparticles: synthesis by the oil-in-water microemulsion reaction method and photocatalytic water-splitting evaluation.* 2019. **44**(24): p. 12421-12429.

87. Zhang, R., et al., *Dielectric and magnetic properties of CoFe2O4 prepared by sol-gel auto-combustion method.* 2018. **98**: p. 133-138.

88. Patterson, A.J.P.r., *The Scherrer formula for X-ray particle size determination.* 1939. **56**(10): p. 978.

89. Li, C., et al., *All polymer dielectric films for achieving high energy density film capacitors by blending Poly (Vinylidene Fluoride-Trifluoroethylene-Chlorofluoroethylene) with aromatic polythiourea.* 2020. **15**(1): p. 1-9.

90. Ng, C., et al., *Structural control of the dielectric, pyroelectric and ferroelectric properties of poly (vinylidene fluoride-co-trifluoroethylene) thin films.* 2020. **22**(4): p. 2414-2423.

91. Zhang, J., et al., *The effect of magnetic nanoparticles on the morphology, ferroelectric, and magnetoelectric behaviors of CFO/P (VDF-TrFE) 0–3 nanocomposites.* 2009. **105**(5): p. 054105.

92. Behera, C., R. Choudhary, and P.R.J.J.o.P.R. Das, *Development of multiferroism in PVDF with CoFe2O4 nanoparticles.* 2017. **24**(4): p. 1-13.

93. Chunyue Li, et al., *"A comparative study on the structural, dielectric, ferroelectric and magnetic properties of CoFe2O4/PbZr0.52Ti0.48O3 multiferroic composite with different molar ratios".* Journal of Physics Communications, 2019. **3.12**.

94. Sapkota, B., et al., *"Fabrication and magnetoelectric investigation of flexible PVDF-TrFE/cobalt ferrite nanocomposite films".* Mater. Res. Express 2022. **49.4**.

95. Kusuma D Y, N.C.A.a.L., *Enhanced ferroelectric switching characteristics of P(VDF-TrFE) for organic memory devices.* J. Phys. Chem. B., 2010. **114, 42**: p. 13289–13293.

96. Sharma, M., J.K. Quamara, and A.J.J.o.M.S.M.i.E. Gaur,, *Behaviour of multiphase PVDF in (1− x) PVDF/(x) BaTiO 3 nanocomposite films: structural, optical, dielectric and ferroelectric properties.* 2018. **9(13)**: p. p. 10875-10884.

97. R.C. Rai, S.W., M. Guminiak, B. Cai, M.L. Nakarmi,, *"Optical and electronic properties of NiFe2O4 and CoFe2O4 thin films".* Appl. Phys. A 106, 2012. **1**: p. 207-211.

98. B. Zhou, Y.W.Z., Y.J. Yu, C.S. Liao, C.H. Yan,, *Correlation between structure and intervalence charge-transfer transitions in nanocrystalline CoFe2 – xMxO4 (M = Mn,Al,Sc) thin films.* Phys.Rev. B 68,, 2003. **2 02446**: p. 024426–024433.

99. Travis Collin Turner, B.S.C., *Synthesis, characterization, and oxygen evolution reaction catalysis of nickel-rich oxides.* diss. 2014, 2014: p. p.62.

100. Bhosale, M.S.S., *Development of Ag/CoFe2O4 Thin Film Memristive Device Using Spray Pyrolysis Technique*. 2018, SCHOOL OF NANOSCIENCE AND BIOTECHNOLGY, SHIVAJI UNIVERSITY, KOLHAPUR (INDIA.

101. Reynolds, N.M.K., K.J.; Chang, C.; Hsu, S.L., *"Spectroscopic analysis of the electric field induced structural changes in vinylidene fluoride/trifluoroethylene copolymers".* Macromolecules 22 1989. **3**: p. 1092–1100.

102. Vadivel, M., Babu, R.R., Ramamurthi, K., Arivanandhan, M.:, *"CTAB cationic surfactant assisted synthesis of CoFe2O4 magnetic nanoparticles".* Ceram. Int. 42,, 2016. **16**: p. 19320–19328.

103. Xuejian Mu, e.a., *"Poly(vinylidene fluoride-trifluoroethylene)/cobalt ferrite composite films with a self-biased magnetoelectric effect for flexible AC magnetic sensors".* J Mater Sci (2021) 56:. **16**: p. 9728–9740

104. Cai K, H.X., Zhao Y, Zong R, Zeng F and GuoD2018, *A green route to a low cost anisotropic MoS2/poly(vinylidene fluoride) nanocomposite with ultrahigh electroactive phase and improved electrical and mechanical properties.* ACS Sustainable Chem. Eng. , 2018. **6.4**: p. 5043–52.

105. Kefeni, K.K., Msagati, T.A.M., Mamba, B.B.:, *Ferrite nanoparticles: synthesis, characterisation and applications in electronic device.* Mater. Sci. Eng. B., 2017. **215** p. 37–55.

106. Dehsari, H.S., *Towards Multi-Ferroic Nanocomposites from Ferroelectric Polymer and Magnetic Nanoparticles.* February 2019: p. 248-249.

107. R.M. Mohamed, M.M.R., F.A. Haraz, W. Sigmund,, *"Structure and magnetic properties of nanocrystalline cobalt ferrite powders synthesized using organic acid precursor method".* J. Magn. Magn. Mater. 322, (2010). **322.14**: p. 2058-2064.

108. Rana DK, S.S., Kundu SK, Roy S, Angappane S, Basu S, *Electrical and room temperature multiferroic properties of polyvinylidene fluoride nanocomposites doped with nickel ferrite nanoparticles.* New J Chem 2019. **43.7**: p. 3128-3138.

109. Mandal, K., Subarna Mitra, and P. Anil Kumar, *"Deviation from Bloch T3/2 law in ferrite nanoparticles".* "EPL (Europhysics Letters), 2006. **75.4**: p. 206-219.

110. Maaz, K.M., A.; Hasanain, S.K.; Bertino, M.F, *Temperature dependent coercivity and magnetization of nickel ferrite particles.* J. Magn. Magn. Mater. **322**: p. 2199-2202.

111. Martins, P., et al., *Applied Surface Science.* 313, Effect of filler dispersion and dispersion method on the piezoelectric and magnetoelectric response of CoFe2O4/PVDF-TrFE nanocomposites: p. 215-219.

112. Martins P, L.A., Gutiérrez J, Barandiarán JM, Orue I and Lanceros-Méndez S 2011, *Effect of filler dispersion and dispersion method on the piezoelectric and magnetoelectric response of CoFe2O4/ P(VDF-TrFE) nanocomposites.* Applied Surface Science 2014. **313**: p. 215-219.

113. GroenouP.FBongersA.LStuyts, A.v., *Magnetism, microstructure and crystal chemistry of spinel ferrites.* Materials Science and Engineering, 1969. **3**: p. 317-392.

114. Hemalatha, P.D.P.a.J., *Enhanced dielectric and ferroelectric properties of cobalt ferrite (CoFe2O4) fiber embedded polyvinylidene fluoride (PVDF) multiferroic composite films.* Mater. Res. Express (2019). **6.9**.